



This is a repository copy of *Modelling the hemodynamics of coronary ischemia*.

White Rose Research Online URL for this paper:

<https://eprints.whiterose.ac.uk/200358/>

Version: Published Version

Article:

Baraikan, A.A. orcid.org/0000-0002-7889-4476, Czechowicz, K., Morris, P.D. orcid.org/0000-0002-3965-121X et al. (11 more authors) (2023) Modelling the hemodynamics of coronary ischemia. *Fluids*, 8 (5). 159. ISSN 2311-5521

<https://doi.org/10.3390/fluids8050159>

Reuse

This article is distributed under the terms of the Creative Commons Attribution (CC BY) licence. This licence allows you to distribute, remix, tweak, and build upon the work, even commercially, as long as you credit the authors for the original work. More information and the full terms of the licence here:

<https://creativecommons.org/licenses/>

Takedown

If you consider content in White Rose Research Online to be in breach of UK law, please notify us by emailing eprints@whiterose.ac.uk including the URL of the record and the reason for the withdrawal request.



eprints@whiterose.ac.uk
<https://eprints.whiterose.ac.uk/>

Modelling The Hemodynamics of Coronary Ischemia

Abdulaziz Al Baraikan ^{1,2}, Krzysztof Czechowicz ¹, Paul D. Morris ¹, Ian Halliday ^{1,*}, Rebecca C. Gosling ¹, Julian P. Gunn ¹, Andrew J. Narracott ¹, Gareth Williams ¹, Pankaj Garg ^{1,3,4}, Maciej Malawski ⁵, Frans van de Vosse ⁶, Angela Lungu ⁷, Dan Rafiroiu ⁷ and David Rodney Hose ¹

¹ Department of Infection, Immunity and Cardiovascular Disease, The Medical School, Sheffield S10 2RX, UK

² College of Applied Medical Sciences, King Saud bin Abdulaziz University for Health Sciences, Riyadh 14611, Saudi Arabia

³ Norwich Medical School, University of East Anglia, Norfolk NR9 3LX, UK

⁴ Norfolk and Norwich University Hospital NHS Foundation Trust, Norfolk NR4 7UY, UK

⁵ Sano Centre for Computational Medicine, 30-072 Krakow, Poland

⁶ Biomedical Engineering Department, Eindhoven University of Technology, 5612AE Eindhoven, The Netherlands

⁷ Department of Electrotechnics and Measurements, Universitatea Tehnica Cluj-Napoca, 400114 Cluj, Romania

* Correspondence: i.halliday@sheffield.ac.uk; Tel.: +44-0114-222-5522

Abstract: Acting upon clinical patient data, acquired in the pathway of percutaneous intervention, we deploy hierarchical, multi-stage, data-handling protocols and interacting low- and high-order mathematical models (chamber elastance, state-space system and CFD models), to establish and then validate a framework to quantify the burden of ischaemia. Our core tool is a compartmental, zero-dimensional model of the coupled circulation with four heart chambers, systemic and pulmonary circulations and an optimally adapted windkessel model of the coronary arteries that reflects the diastolic dominance of coronary flow. We guide the parallel development of protocols and models by appealing to foundational physiological principles of cardiac energetics and a parameterisation (stenotic Bernoulli resistance and micro-vascular resistance) of patients' coronary flow. We validate our process first with results which substantiate our protocols and, second, we demonstrate good correspondence between model operation and patient data. We conclude that our core model is capable of representing (patho)physiological states and discuss how it can potentially be deployed, on clinical data, to provide a quantitative assessment of the impact, on the individual, of coronary artery disease.

Keywords: haemodynamics; compartmental models; parameter identification; fluid dynamics



Citation: Baraikan, A.A.; Czechowicz, K.; Morris, P.D.; Halliday, I.; Gosling, R.C.; Gunn, J.P.; Narracott, A.J.; Williams, G.; Garg, P.; Malawski, M.; et al. Modelling The Hemodynamics of Coronary Ischemia. *Fluids* **2023**, *8*, 159. <https://doi.org/10.3390/fluids8050159>

Academic Editors: Huidan (Whitney) Yu and D. Andrew S. Rees

Received: 7 February 2023

Revised: 6 April 2023

Accepted: 27 April 2023

Published: 17 May 2023



Copyright: © 2023 by the authors. Licensee MDPI, Basel, Switzerland. This article is an open access article distributed under the terms and conditions of the Creative Commons Attribution (CC BY) license (<https://creativecommons.org/licenses/by/4.0/>).

1. Introduction

Myocardial function is dependent on sufficient coronary blood flow (CBF), the rate of which is matched closely to the fluctuating metabolic requirements of the heart. CBF is compromised in ischaemic heart disease (IHD), the commonest cause of death in the world. The most frequent cause of IHD is coronary artery disease (CAD), whereby the epicardial coronary arteries become stenosed or occluded, thus restricting CBF, initially under exercise conditions, but eventually at rest; see Section 3.2.2. Although there are data correlating global myocardial ischaemic burden with clinical outcomes, there are little data linking it with myocardial energetics, function or cardiac output. Here we demonstrate a multi-compartment, zero-dimensional (0D) model [1–4] of the coronary and systemic circulation, based on clinical data, with the potential to address myocardial energetics. Specifically, we postulate that a zero-dimensional (0D) model, adapted to readily available, patient-specific data, can accurately simulate coronary (patho)physiology, with the potential to personalise [5] and predict an individual patient's global ischaemic burden and associate this with LV energetics and cardiac output. Our aims are to:

1. Devise and implement a 0D model and robust data handling protocols able to replicate *in silico* haemodynamic dysfunction;
2. Make optimal use of appropriate haemodynamic data, collected in the clinical PCI pathway;
3. Demonstrate our process' ability to capture patient-specific (patho)physiological states *in silico*.

2. Background

CFD modelling can provide a detailed assessment of local, usually single-vessel coronary haemodynamics which may be patient-specific [6]. It has also allowed for less or even non-invasive diagnostic tools, such as virtual fractional flow reserve (vFFR) [7], and in the novel form of the lattice Boltzmann simulation [8], it may be extended to describe flow within multiple small vessels [9]. However, CFD alone cannot provide a description of the perfusion of the entire myocardium necessary to characterise global ischaemic burden. To quantify the effects of multi-vessel disease upon total myocardial blood flow, one must set the diseased vessel(s) within the context of the whole coronary tree. This requires a methodology which can interact with CFD *and* wider physiological data.

Windkessel models are not new [10,11], neither are low-order representations of cardiac function [12–14] and coupled pseudo-mechanical system models, which have both been utilised here have been available, open source, for years [15]. We are concerned with computational medicine however, where a parsimonious model design should be constrained by data sources, with suitable interpretation protocols in mind. A composite of low-order models comprising a mechanical cardio-vascular 0D model of left heart function, valvular function and systemic circulation has been shown to have the capacity to ingest CFD-derived data and prognose the systemic effects of aortic and mitral valve disease [16]. Czechowicz et al. took CFD-derived valve properties, ingested them into a 0D model and formulated hypotheses connecting valve physiology, personalised cardiac energetics and valve function, to develop a clinical decision support tool. Here, we attempt to extend that methodology to a wider range of clinical data and disease states which are more difficult to characterise. This requires:

1. A coronary network topology conforming to the clinical pattern of atherosclerosis;
2. Modelling that reflects diastolic dominance of myocardial flow;
3. The ability to incorporate all available clinical patient data;
4. Sufficient computational simplicity for clinical deployment.

These demands make it necessary to simplify the task from the outset. To reduce the burden of model personalisation, we parameterise its right circulation parameters to normal values [17]. (This decision is supported by our input parameter sensitivity analysis in Appendix B, which shows that the coronary, left heart and systemic circulation input parameters are most influential). Further, the fact that resting coronary blood flow (250 mL min^{-1} ; $0.8 \text{ mL min}^{-1} \text{ g}^{-1}$ of heart muscle) constitutes about 5% of cardiac output [18] allows us to assume that coronary flow does not directly influence the systemic circulation. It also allows us to approach our problem by adjusting, with the relevant coronary flow data *a posteriori*, a model in which systemic and ventricular outputs are tuned first. Further, we appeal, hierarchically, to the key physiological principles of LV performance and the systemic circulation to construct each patient's baseline and only then incorporate detailed CFD-derived information related to the coronaries' microvascular resistance (MVR), etc., while retaining a minimum number of assumptions necessary to impose physiological principles. We use cardiac energetics and the concepts encapsulated in Wiggers' diagram [19] to refine our low-order model of LV contractility and compliance; then, we consider ventricular–aortic (VA) coupling (which characterises the interaction between the myocardial contractile function and LV afterload and defines cardiovascular performance and efficiency [20]), and finally, the role of passive ventricular filling and valves. Only once an accurate model of general cardiac function is established will coronary flow be considered.

3. Methods and Materials

Broadly, we first describe our model (Section 3.1), then its data (Section 3.2). However, since model operation and data are related, some model details bleed into Section 3.2.

3.1. Methods

Personalisation cost function hyper-surfaces are intricate in the presence of non-linearities. Similar to valve functions, the cost function varies at very different rates with displacement in different parameter directions. Then, the task of locating the global minimum becomes computationally expensive. We address this difficulty with the multi-step protocol outlined in Table 1. The six steps declared there buffer clinical data into our tool, using low-order haemodynamic models, a closed loop system model and finally 3D CFD.

3.1.1. Low-Order Models

To express heart chamber biomechanics and valve characteristics appropriately, we use the double Hill elastance model [12,14] and the valves' pressure-flow characteristics. See Appendix A.2 for details; see also Czechowicz et al. [16], who give a fuller account of valve characteristic functions. Our passive systemic and pulmonary circulation windkessels, with proximal inertance (L), viscous dissipation (R) and multiple compliance (C), are also well documented [21]. Our pulmonary and systemic windkessels are designated LRCRC, having two capacitances to separate arterial and venous compliance. Note, each coronary branch is characterised by a compliance with its back plate pressure set to that in the relevant ventricle. Note also that elastance is not used solely to activate our system model. We will also use it, together with the LV PV loop [22], to clarify the relationship between our LV pressure and volume time-series data in Section 3.2.1.

3.1.2. System Model

Figure 1 shows, in relation to our CFD models, our assembly of windkessels, elastance functions and valves. It is designated a compartmental, electrical analogue or 0D model. It has four heart chambers as well as systemic arterial and venous, pulmonary arterial and venous, and several coronary arterial compartments. The overhead of four heart chambers is offset by enhanced performance [17]. We set the right circulation parameters to population average values. We compute N sampled time-series outputs $y_n(t_i)$, $n = 1, \dots, N$, derived from internal states, $x_n(t_i)$, $n = 1, \dots, N$ with the sample times t_i drawn from the converged heart cycle. Table 2 declares our compartment numbering convention and Table 3 our names, conventions, equivalent subscripting and input parameter base values. Note, micro-vascular resistance (MVR) is distributed relative to arterial compliance, with a proximal-to-distal ratio controlled by input parameter α .

It is typical to express the dynamics of the system in Figure 1 in coupled ordinary differential equations (ODEs), or differential algebraic equations (DAEs [23]), typically with compartment pressures serving as internal states. In state-space form [24], using relative time, our model is expressed as

$$\frac{dx}{d\tau} = \underline{f}(x(\tau); \Theta), \quad y(\tau) = \underline{h}(x(\tau); \Theta),$$

Vector function $\underline{h}(\ast)$, which maps between internal states and outputs, is often the identity. Outputs $\underline{y}(\tau)$ can, of course, be sampled to generate a discrete output metrics vector. Θ denotes the system model's full input parameter set and

$$x(\tau) = (p_1(\tau), p_2(\tau), \dots, p_{10}(\tau))^T.$$

is our instantaneous state vector. We use $\Theta(\theta)$ to denote the full set (a subset) of input parameters. Particular examples of the system expressed in equations in Section 3.1.2 are given in Appendix A. Deriving equations in Section 3.1.2 uses recursive applications

of simple haemodynamic sub-models, to formulate, in closed form, all the necessary relationships between compartmental pressures, volumes and flows (see Appendix A). A simple but lengthy process of eliminating flow and volume variables results in a DAE system [23] which is readily transformed into state-space form, by differentiating equations where necessary. Typically, the system is solved using a time-marching numerical solution, e.g., a fourth-order Runge–Kutta algorithm. A time step of 1×10^{-3} was chosen for the numerical solution. It will occasionally be helpful to replace the numerical compartment index (subscript) with an abbreviation of its name, e.g., $p_1(t) = p_{LV}(t)$, with LV denoting left ventricle, etc.; see Tables 2 and 3. For example model output data see Figure 2, which shows flow in a coronary artery illustrating a key feature- to capture diastolic dominance in coronary flow, our coronary vessels’ compliance is biased by the LV or RV pressure, as appropriate.

Table 1. Stages in the personalisation process and their rationale. Physiological effects (column 2) are sequentially ingested into the workflow, with the objective declared in column 3, culminating, at step 5, in a patient-specific in silico model of the resting patient state.

Step	Processing Tool	Physiology	Objective	Comment
0	statistical analysis	LV function	ensemble average, downsample time-series	synchronised to ECG1 R-R interval
1	elastance model	LV function	derive LV elastance; ingest into 0D model	characterised by double Hill LV parameters
2	0D system model	LV–aortic coupling in systole	primary tune of 0D model systemic circulation windkessel parameters	large sub-space scanned by GA tuning
3	0D system model	LV–atrial coupling and diastolic filling	ancillary tuning of 0D left atrial elastance and mitral valve resistances	uses gradient descent tuning.
4	CFD analysis	coronary flows	ingest into 0D model computed R_{sten} , MVR	use software VirtuHEART™
5	0D system model	system-coronary	in silico representation of the patient at rest	

Table 2. Indexing and naming conventions for system model variables. Free subscript * is to be replaced by the appropriate symbol. Flows generally are trans-compartment; pressures and volumes apply to compartments directly.

Number	Subscript	
	$p_*(t), v_*(t)$	$q_*(t)$
1	LV	ao val
2	RA	tri val
3	RV	pul val
4	LA	mit val
5	sys art	sys prox
6	pul art	pul prox
7	sys ven	sys dist
8	pul ven	pul dist
9	cor art	cor prox
10	cor ven	cor dist

Table 3. System model input parameter nomenclature and status. The 0D model chamber parameters are classified by compartment. The status of the parameter is either fixed (at population average value) or tuned, from an initial value declared above. In the latter, the step in which the parameter is tuned is identified below. Note, the coronary LAD circulation parameters 74, . . . , 80 and the coronary RCA circulation parameters 81, . . . , 87 follow the naming convention of those declared above for the left circumflex artery, with the text “LAD” and “RCA” replacing the text “Cx” and identical initialisations.

Compartment	Index	Symbol	Description	Unit	Status	Base Value	
NA	1	HR	Heart rate	bpm	Allocated		
NA	2	mcfp	Mean circulatory filling pressure	mmHg	tuned, step 3	7	
Left Ventricle (LV)	3	$E_{LV,min}$	LV min. elastance (“compliance”)	mmHg/mL	assigned, step2	0.08	
	4	$E_{LV,max}$	LV max. elastance (“contractility”)	mmHg/mL	assigned, step3	3	
	5	$n_{LV,1}$	LV contraction rate constant	-	tuned, step 2	1.32	
	6	$n_{LV,2}$	LV relaxation rate constant	-	tuned, step 2	27.4	
	7	$\tau_{LV,1}$	LV systolic time constant	-	tuned, step 2	0.269	
	8	$\tau_{LV,2}$	LV diastolic time constant	-	tuned, step 2	0.452	
	9	$V_{LV,0}$	LV volume offset	mL	fixed	10	
	10	$T_{LV,shift}$	LV fractional time shift	-	fixed	0	
	Left Atrium (LA)	11	$E_{LA,min}$	LA max. elastance (“compliance”)	mmHg/mL	tuned, step 4	0.08
		12	$E_{LA,max}$	LA min. elastance (“contractility”)	mmHg/mL	tuned, step 4	0.17
13		$n_{LA,1}$	LA contraction rate constant	-	fixed	1.32	
14		$n_{LA,2}$	LA relaxation time constant	-	fixed	13.1	
15		$\tau_{LA,1}$	LA systolic time	-	tuned, step 4	0.11	
16		$\tau_{LA,2}$	LA diastolic time	-	tuned, step4	0.18	
17		$V_{LA,0}$	LA volume offset	mL	fixed	3	
18		$T_{LA,shift}$	LA fractional time shift	-	fixed	0.85	
Right Ventricle (RV)	19	$E_{RV,min}$	RV min. elastance (“compliance”)	mmHg/mL	fixed	0.04	
	20	$E_{RV,max}$	RV max. elastance (“contractility”)	mmHg/mL	fixed	0.6	
	21	$n_{RV,1}$	RV contraction rate constant	-	fixed	1.32	
	22	$n_{RV,2}$	RV relaxation rate constant	-	fixed	27.4	
	23	$\tau_{RV,1}$	RV systolic time	-	fixed	0.269	
	24	$\tau_{RV,2}$	RV diastolic time	-	fixed	0.452	
	25	$V_{RV,0}$	RV volume offset	mL	fixed	55	
	26	$T_{RV,shift}$	RV fractional time shift	-1	fixed	0	
Right Atrium (RA)	27	$E_{RA,min}$	RA max. elastance (“compliance”)	mmHg/mL	fixed	0.04	
	28	$E_{RA,max}$	RA min. elastance (“contractility”)	mmHg/mL	fixed	0.15	
	29	$n_{RA,1}$	RA contraction rate constant	-	fixed	1.32	
	30	$n_{RA,2}$	RA relaxation rate constant	-	fixed	13.1	
	31	$\tau_{RA,1}$	RA systolic time	-	fixed	0.11	
	32	$\tau_{RA,2}$	RA diastolic time	-	fixed	0.18	
	33	$V_{RA,0}$	RA volume offset	mL	fixed	17	
	34	$T_{RA,shift}$	RA fractional time shift	-	fixed	0.85	
Systemic Circulation LR CRC windkessel	35	$R_{sysart,dist}$	Systemic Resistance Distal	mmHg·s/mL	tuned, step 3	0.033	
	36	$R_{sysart,prox}$	Systemic Resistance Proximal	mmHg·s/mL	tuned, step 3	0.9	
	37	$C_{sysart,prox}$	Systemic Arterial Proximal Capacitance	mL/mmHg	tuned, step 3	1	
	38	$V_{sysart,prox,0}$	Systemic Arterial Proximal Unstressed Volume	mL	fixed	720	
	39	$C_{sysart,dist}$	Systemic Arterial Distal Capacitance	mL/mmHg	fixed	11	
	40	$V_{sysart,dist,0}$	Systemic Arterial Distal Unstressed Volume	mL	fixed	3000	
	41	$L_{sysart,prox}$	Systemic Arterial Inertance (Proximal)	mmHg·s ² /mL	tuned, step 3	0.005	

Table 3. *Cont.*

Compartment	Index	Symbol	Description	Unit	Status	Base Value
Pulmonary Circulation LR CRC windkessel	42	$R_{pulart,dist}$	Pulmonary Resistance Distal	mmHg·s/mL	fixed	0.01
	43	$R_{pulart,prox}$	Pulmonary Resistance Proximal	mmHg·s/mL	fixed	0.05
	44	$C_{pulart,prox}$	Pulmonary Arterial Proximal Capacitance	mL/mmHg	fixed	10
	45	$V_{pulart,prox,0}$	Pulmonary Arterial Proximal Unstressed Volume	mL	fixed	180
	46	$C_{pulart,dist}$	Pulmonary Arterial Distal Capacitance	mL/mmHg	fixed	15
	47	$V_{pulart,dist,0}$	Pulmonary Arterial Distal Unstressed Volume	mL	fixed	720
	48	$L_{pulart,prox}$	Pulmonary Arterial Inertance (Proximal)	mmHg·s ² /mL	fixed	0.0017
	Aortic Valve	49	$a_{2,aortic}$	Aortic Valve quadratic coefficient	mmHg·s ² /mL ² mL	fixed
50		$a_{1,aortic}$	Aortic Valve linear coefficient	mmHg·s/mL	fixed	0
51		$a_{2,aortic,regurg}$	Aortic Valve regurgitant quadratic coefficient	mmHg·s ² /mL ² mL	fixed	0
52		$a_{1,aortic,regurg}$	Aortic Valve regurgitant linear coefficient	mmHg·s/mL	fixed	0
Mitral Valve	53	$a_{2,mitval}$	Mitral Valve quadratic coefficient	mmHg·s ² /mL ² mL	tuned, step 4	6.25×10^{-6}
	54	$a_{1,mitval}$	Mitral Valve linear coefficient	mmHg·s/mL	tuned, step 4	0
	55	$a_{2,mitval,regurg}$	Mitral Valve regurgitant quadratic coefficient	mmHg·s ² /mL ² mL	fixed	0
	56	$a_{1,mitval,regurg}$	Mitral Valve regurgitant linear coefficient	mmHg·s/mL	fixed	0
Pulmonary Valve	57	$a_{2,pulval}$	Pulmonary Valve quadratic coefficient	mmHg·s ² /mL ² mL	fixed	8.16×10^{-6}
	58	$a_{1,pulval}$	Pulmonary Valve linear coefficient	mmHg·s/mL	fixed	0
	59	$a_{2,pulval,regurg}$	Pulmonary Valve regurgitant quadratic coefficient	mmHg·s ² /mL ² mL	fixed	0
	60	$a_{1,pulval,regurg}$	Pulmonary Valve regurgitant linear coefficient	mmHg·s/mL	fixed	0
Tricuspid Valve	61	$a_{2,trival}$	Tricuspid Valve quadratic coefficient	mmHg·s ² /mL ² mL	fixed	6.25×10^{-6}
	62	$a_{1,trival}$	Tricuspid Valve linear coefficient	mmHg·s/mL	fixed	0
	63	$a_{2,trival,regurg}$	Tricuspid Valve regurgitant quadratic coefficient	mmHg·s ² /mL ² mL	fixed	0
	64	$a_{1,trival,regurg}$	Tricuspid Valve regurgitant linear coefficient	mmHg·s/mL	fixed	0
Coronary Left Main	65	$a_{2,LMart,regurg}$	Left main stenosis, quadratic coefficient	mmHg·s ² /mL ²	assigned, step 5	0
	66	$a_{1,LMart,regurg}$	Left main stenosis, linear coefficient	mmHg·s/mL	assigned, step 5	0
Coronary Circumflex RCRC windkessel	67	$a_{2,Cx,art}$	Circumflex, quadratic coefficient	mmHg·s ² /mL ² mL	assigned, step 5	0
	68	$a_{1,Cx,art}$	Circumflex, linear coefficient	mmHg·s/mL	assigned, step 5	0
	69	$R_{Cx,MVR}$	Circumflex, RCR total resistance	mmHg·s/mL	assigned, step 5	35
	70	C_{Cx}	Circumflex, RCR capacitance	mL/mmHg	tuned, step 5	0.25
	71	α_{Cx}	Circumflex, RCR fraction proximal resistance	-	tuned, step 5	0.9
	72	$V_{Cx,0}$	Circumflex unstressed volume	mL	tuned, step 5	8
	73	β_{Cx}	Circumflex capacitance back pressure fraction	-	fixed	0.5

3.1.3. Input Parameters, Local Sensitivity and Orthogonality Analysis

Of our 87 input parameters, a majority take population average values and are not tuned; see Table 3. The interrogated input parameter sub-space is spanned by parameters of cardiac energetics, coronary perfusion, LV and left atrial elastance, the mitral valve, the coronary and systemic windkessels and mean circulatory filling pressure. The underlying full local sensitivity and input parameter orthogonality analysis is shown in Appendix B, along with a reduced analysis, based upon the most relevant inputs and outputs.

3.1.4. Model Personalisation or Input Parameter Identification

Personalisation involves inverse operation, guided by a cost function, together with an appropriate multi-variate functional minimisation algorithm. Our personalisation process

is multi-stage. It is summarised in the inter-relating Tables 1, 4 and 5. For all stages, the minimised cost function is a scalar weighted composite of: (i) the L^2 norm of the difference between model-predicted and target data interpolated onto the same times, t_i , and (ii) a derived metric, Y_n

$$f(\Theta) = \sum_{j=1}^M \left(w_j^{(1)} \left\{ \sum_{i=1}^N \left(y_j(\underline{x}(t_i; \Theta)) - y_j^{target}(t_i) \right)^2 \right\} + w_j^{(2)} Y_n^2 \right). \tag{1}$$

For example, a derived metric might be systolic systemic arterial (compartment 5) pressure

$$Y_5 = \max_{t_i} (p_5(t_i; \Theta)) - \max_t (p_5^{target}(t)),$$

with $w_j^{(1)}$ and $w_j^{(2)}$ denoting the weights. We defer further discussion until Section 3.2.

Having summarised our processing and its rationale and declared our notation, we may now conclude this sub-section by defining the processing in key steps 3 and 4 of our protocol, which require inverse operation, or tuning, of the 0D system model. In Table 6 we state the model input parameters which are tuned and the corresponding patient data that is used to perform the tuning in each of the steps 3 and 4.

Table 4. Patient-specific data. Data are classified according to physical and mathematical significance, how the data are used, patient state and the 0D model compartment(s) to which they apply. Table 5 provides more information on the sub-models used to introduce these data into our 0D system model. The free subscript * in column 6 denotes one of the resolved coronary arteries, LMS (left main stem), LCA (left coronary artery), LCX (left circumflex) and RCA.

Data Source	Compartment	Role	Unit	Data Form	Notation	State			Pathway Stage	
						Rest	Exercise	Hyperemia	Pre PCI	Post PCI
six-minute walk test	all (general)	cardiac output proxy	~	statistics	~	yes	yes	no	yes	yes
activity monitoring	all (general)	cardiac output proxy	~	statistics	~	yes	yes	no	yes	yes
CMR scan	left ventricle	volume	ml	time-series	$v_{LV}(t)$	yes	no	no	yes	no
coronary angiograms	coronaries	flow	mL/s	discrete	$\langle Q_* \rangle_t$	yes	no	yes	yes	yes
coronary angiograms	coronaries	MVR	mmHg·s/mL	discrete	$R_{\mu LCA}$ etc.	yes	no	yes	yes	yes
PCI pressure catheter	left ventricle	pressure	mmHg	time-series	$p_{LV}(t)$	yes	no	yes	yes	yes
PCI pressure catheter	systemic	pressure	mmHg	time-series	$p_{AO}(t)$	yes	no	yes	yes	no
PCI pressure catheter	coronaries	pressure	mmHg	time-series	$p_*(t)$ etc.	yes	no	yes	yes	yes

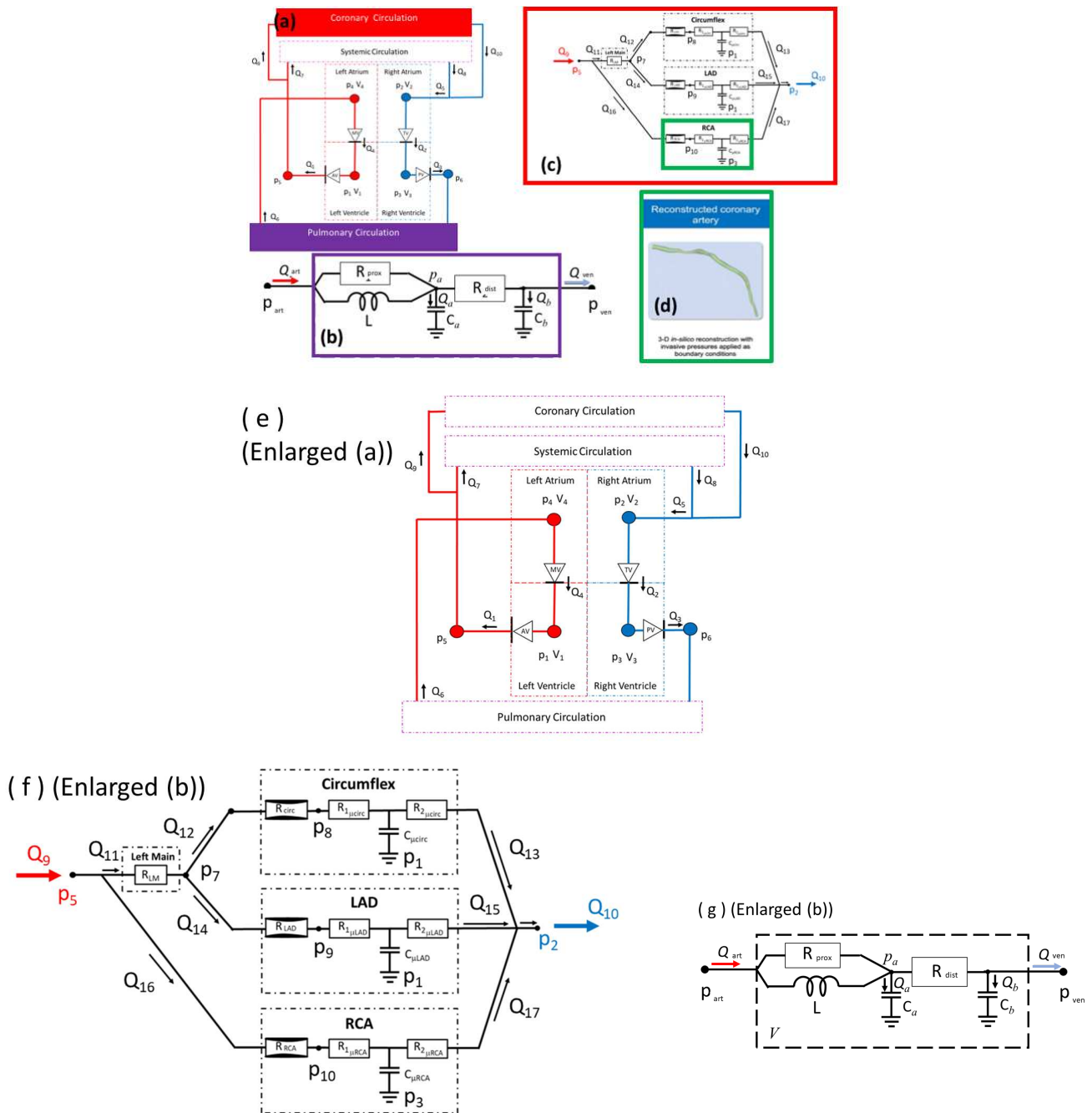


Figure 1. Interacting 0D system and CFD models. Clockwise from the top. First panel uses colour coding to expose the interaction between (a) core heart module; (b) systemic and LRCRC windkessels; (c) coronary module; and (d) 3D steady CFD workflow used to parameterise the stenotic resistance and MVR. (e) An enlargement of (a), the heart module. Important pressure, flow and volume variables are displayed. Valves are all diodes. Chamber elastances are represented by double Hill elastance functions. The subscripting of the compartment state variables (p_n, v_n, q_n), $n = 1, \dots, 10$ is that which is used throughout, with the convention that compartment, inlet pressure, volume and outlet flow are all subscripted by the compartment number. (f) An enlargement of (c), the coronary windkessel set. There is a RCR windkessel for each of the three principal vessels, designated LCx, LAD and RCA. The back plates of the vessel compliances are all coupled to the relevant ventricular pressure. (g) An enlargement of (b), the systemic and pulmonary circulation windkessels.

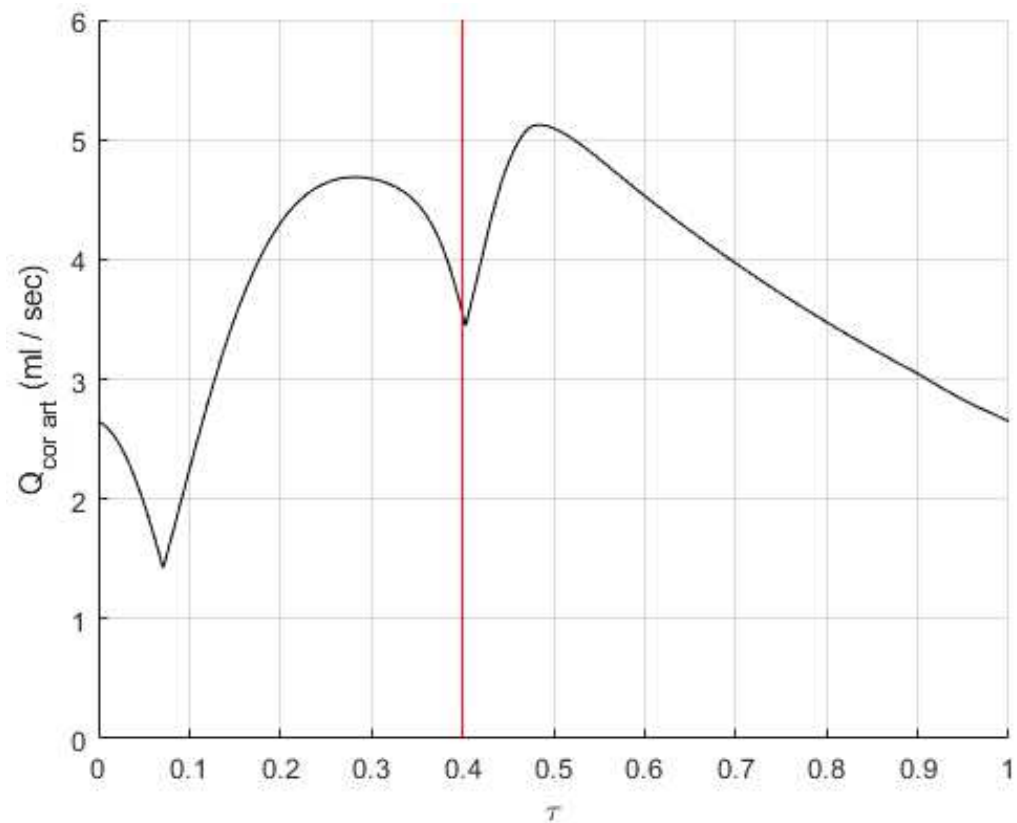


Figure 2. Diastolic dominance of coronary artery flow in the system model. It is essential to capture the diastolic dominance of flow in the coronaries. Here, the vertical red line indicates the end of systole. These illustrative data show that computed flow peaks in the diastolic phase.

Table 5. Sub-models used to pre-process patient data. We provide further information on how patient data outlined in Table 4 are prepared. Here, $\langle \cdot \rangle_{EA}$ denotes an ensemble average, taken over equivalent intervals of dimensionless time τ . This table shows the interaction between the various data sources and re-processing, to allow them to be ingested into the 0D compartmental system model (column 3). All pressure data were downsampled onto the CMR phase times; see Equation (2).

Source Data	Pre-Processing	Ingests into 0D System Model as
$\langle v_{LV}(\tau) \rangle_{EA}$	fit to double Hill elastance function	personal elastance function parameters
$\langle p_{LV}(\tau) \rangle_{EA}$		
$\langle v_{LV}(\tau) \rangle_{EA}$	extract extrema	personal LV volume extrema
$\langle p_{LV}(\tau) \rangle_{EA}$	extract extrema	personal LV pressure extrema
$\langle p_{AO}(\tau) \rangle_{EA}$		personal systemic (aortic) pressure time-series
coronary angiograms	steady-state CFD simulations	personal MVRs for treated vessels
$\langle p_{LMS}(\tau) \rangle_{EA}$ etc.		
coronary angiograms	steady-state CFD simulation	personal stenotic Bernoulli resistance quadratic and linear coefficients in treated vessels
$\langle p_{LMS}(\tau) \rangle_{EA}$ etc.		
6mwt	clinical interpretation	validation data
monitoring		

Table 6. Supplementary information for Table 1. Additional information on personalisation steps 3, 4, declared in Table 1. The search target data and input parameter sub-space are identified here. Note that search targets accumulate between steps 3 and 4.

Step	Personalisation Search Definition	
	Input Parameters Adjusted	Output Metrics Targeted
3	$mcfp, L, R_{prox}, R_{dist}, C_{prox}$	$\max_{\tau}(v_{LV}(\tau)), \min_{\tau}(v_{LV}(\tau)), \max_{\tau}(p_{LV}(\tau)), \min_{\tau}(p_{LV}(\tau)), \{p_{AO}(\tau_i); i = 1, \dots, 29\}$
4	$a_{1,mit}, a_{2,mit}, n_1^{LA}, n_2^{LA}, \tau_1^{LA}, \tau_2^{LA}, E_{LA,max}, E_{LA,min}$	to the above, add $\{v_{LV}(\tau_i); i = 1, \dots, 29\}$

3.1.5. 3D CFD Models

We proceed to consider the CFD tools and modelling used in our study. Patient-specific stenotic Bernoulli resistance coefficients and MVRs are provided in our core model using two validated CFD based methods, (i) VirtuHEART™ (University of Sheffield, Sheffield, United Kingdom) and (ii) VirtuQ™ (University of Sheffield, Sheffield, United Kingdom) [6,7]. In the domain Ω , these tools solve the incompressible Navier–Stokes and continuity equations

$$\begin{aligned} (\underline{v}(\underline{r}) \cdot \nabla) \underline{v}(\underline{r}) &= -\frac{1}{\rho} \nabla p(\underline{r}) + \nu \nabla^2 \underline{v}(\underline{r}), \\ \nabla \cdot \underline{v}(\underline{r}) &= 0, \end{aligned} \tag{2}$$

for steady, i.e., time-average flow; all symbols have their usual meaning. An accepted approximate value of Reynolds’ number $Re \approx 600$ for the coronary arteries, which indicates transitional flow. Note that we assume blood is a Newtonian fluid. Patient-specific boundary conditions are derived as follows. A closed coronary artery geometry (Figure 1d) is decomposed into a luminal boundary, $\partial\Omega_1$, an entrance face, $\partial\Omega_2$, and an exit face, $\partial\Omega_3$. Using epipolar geometry and two compatible angiogram views, taken at the time of PCI, we construct $\partial\Omega_1$, generate a mesh and apply a Dirichlet, no-slip condition

$$\underline{v}(\underline{r}) = 0, \quad \underline{r} \in \partial\Omega_1.$$

We remark that a model of vessel sequestration using Murray’s law [25,26] to assign a flux across the luminal boundary based upon local geometry is available [7,27]; however, zero leak was specified here. Lesion proximal and distal time-averaged pressures are also recorded at PCI. Solutions were computed using Fluent™ (Ansys Corporation, Canonsburg, PA, United States of America), with boundaries $\partial\Omega_2$ and $\partial\Omega_3$ processed in each of two ways:

1. Following VirtuQ methodology, apply measured proximal and distal average pressure on $\partial\Omega_2, \partial\Omega_3$, respectively,

$$p(\underline{r}) = \langle p_{*,prox}(\tau) \rangle_{\tau}, \quad \underline{r} \in \partial\Omega_2; \quad p(\underline{r}) = \langle p_{*,dist}(\tau) \rangle_{\tau}, \quad \underline{r} \in \partial\Omega_3,$$

we compute the steady-state solution and deduce vessel flow

$$q_* = \int \int_{\partial\Omega_3} \underline{v}(\underline{r}) \cdot d\underline{A};$$

then, we use Ohm’s law and $\langle p_{*,dist}(\tau) \rangle_{\tau}$ to compute a patient-specific MVR.

2. Following VirtuHeart methodology, assume an MVR based on patient characteristics [6]; compute vessel inlet and outlet areas

$$A_{in} = \int \int_{\partial\Omega_2} dA, \quad A_{out} = \int \int_{\partial\Omega_3} dA,$$

set two physiologically plausible inlet flows ($q_* = 1, 3 \text{ mL/s}$), find uniform inlet and outlet streamwise velocities

$$v_s^{in}(\underline{r}) = \frac{q_*}{A_{in}}, \quad \underline{r} \in \partial\Omega_2; \quad v_s^{out}(\underline{r}) = \frac{q_*}{A_{in}}, \quad \underline{r} \in \partial\Omega_3,$$

compute the two corresponding pressure drops, $\delta p_*^1, \delta p_*^3$ and hence infer the two Bernoulli resistance coefficients of the stenosis.

3.2. Materials

We analysed anonymised clinical datasets from 40 CAD patients with angina symptoms. The elective PCI workflow culminates in re-vascularisation of one or more of the coronaries in a majority of cases. The decision to stent is guided by the average pressure drop across a lesion. This is measured using a pressure wire (PRESSUREWIRE™X Abbott, downloading software Coroflow™, Coroventis Uppsala, Sweden) with the patient in a hyperaemic state of pharmacological stress induced by adenosine (a strong vasodilator); from this, one computes

$$FFR = \frac{P_{distal}}{P_{proximal}}, \tag{3}$$

with re-vascularisation indicated for $FFR < 0.8$. The clinical pathway generates PCI pressure data, cardiac MRI of the LV, six-minute walk tests (6mwt) before and after PCI and home activity monitoring (see below); these data fall into two categories

1. Measured data (such as pressure and volume, expressed as time-series);
2. Exercise and physical activity data (like patient 6mwt (exercise) and home monitoring (activity) measures).

Table 4 identifies data available for every patient, for Table 5, the particular form in which pre-processed data modalities, declared in Table 4, are ingested into the system model, and Table 1, a commensurate sequence of handling protocols.

Our personalisation process steps $0, \dots, 5$ (Table 1) introduce physiological effects sequentially, considering

1. Functional form (qualitative data trends should accord with accepted physiology);
2. Modality (pressure is measured directly, using a manometer; CMR volumes, in contradistinction, involve reciprocal space reconstruction).

Our raw data take the form of time-series at two sampling rates. Pressure data were all sampled for 120 s, using a sampling rate of 100 Hz. CMR volumes were acquired at a nominal sampling rate of 30 images per heart cycle. Pressure and volume can be co-registered to the start of ventricular contraction using the RR interval of the concurrent ECG1 traces, also recorded. Pressure and CMR data were acquired at different stages in the patient pathway (Table 4), with patients often in different physiological states. For all pressure signals, the sampled wave-train had its low frequency contribution removed and was decomposed, using time-domain analysis, into single beat pressure excursions, identified from the concurrent ECG 1 R-R interval, and then ectopic beats were filtered, and the remaining cycle pressure samples were downsampled onto the 30 dimensionless times defined as follows

$$\tau_n = \frac{n}{30} \tau, \quad n \in \mathbb{N}, \quad 0 \leq n \leq 29; \quad \tau = \frac{t}{T}, \quad T = \frac{60}{HR}, \tag{4}$$

corresponding to CMR data sampling times. This set was then ensemble averaged, with the sample standard deviations in each dimensionless time channel providing an error. Example aortic and LV pressure data are shown in Figure 3. CMR-derived LV volume data are also effectively ensemble averaged (acquisition involves a reciprocal space reconstruction of data acquired at a given cycle phase, over several consecutive beats). Our CMR total LV volume measurements are attributed to 30 equispaced dimensionless times. Each was computed by segmenting the chamber, in a set of between 9 and 12 cross-sections, with

the base and apical frames frequently discarded, owing to error. Frames were positioned along the long axis of the approximately cylindrical LV. Our segmentation and subsequent volume computation were performed using the MASS™ software (Leiden University, Version 2018 EXP, Leiden University Medical Centre, Leiden, The Netherlands). Figure 3, right panel, shows a typical CMR volume time-series.

Downsampled pressure and volume are acquired relative to a common clock provided by the ECG 1 RR interval which can potentially synchronise them, to yield a personal double Hill elastance function, $E_{LV}(t)$, etc. However, there are demonstrable inconsistencies, such as heart rate (HR) miss-match. Pressure data have a certain HR, and CMR data another. We will demonstrate that careful pressure and volume time-series co-registration is essential, and we will develop a minimal rigid shift which adjusts only relative phase.

3.2.1. Physical Data Processing

Chamber elastance functions (Appendix A.2) are low-order models developed from studied physical data. Elastance may be defined as follows

$$E_*(\tau) \equiv \frac{p_*(\tau)}{(v_*(\tau) - v_0)}, \tag{5}$$

where subscript * now denotes the chamber and v_0 its unstressed volume. We take the clinical approximation, $v_0 = 0$. Clearly in Equation (5), $E_*(\tau)$ is sensitive to the relative phase of $p_*(\tau)$ and $v_*(\tau)$, but the importance of co-registration is perhaps better illustrated by another metric—the PV loop. The latter is a closed, two-dimensional parametric, Cartesian curve

$$(p_{LV}(\tau), v_{LV}(\tau)), \quad \tau \in [0, 1].$$

Figure 4, top panel, shows a personal PV loop in which the LV pressure and volumes are correctly co-registered. The ventricular–aortic coupling parameter (blue line) and the wasted mechanical work, as well as the useful mechanical work (loop area), can be deduced. In contradistinction, Figure 4, bottom panel, shows the same patient’s PV loop using the putative common clock of the RR interval, to co-register the two time-series signals (red data). This *primitive* co-registration is implausible: it has no identifiable iso-volumetric phases, and it implies a high level of valvular regurgitation and irregular aortic and mitral valve actuation pressures. The difference between Figure 4, top and bottom panels, argues for a principled co-registration other than the ECG 1 RR signal. Reserving for subsequent work a more elaborate co-registration, possibly involving signal dilations, we chose rigidly to delay the LV volume samples $\{v_{LV}(\tau_n), 0 \leq n \in \mathbb{N}, n \leq 29\}$ relative to a fixed pressure sample set $\{p_{LV}(\tau_n), n \in \mathbb{N}, n \leq 29\}$, by an integral number of dimensionless time steps, $\delta\tau = (\tau_n - \tau_{(n-1)})$. We observed a cohort-average shift of two CMR phases. Patient-specific synchronisation was accomplished by seeking the instant at which the aortic and mitral valves open, in the separate pressure and volume time-series, using the multiple criteria declared in the fourth column of Table 7.

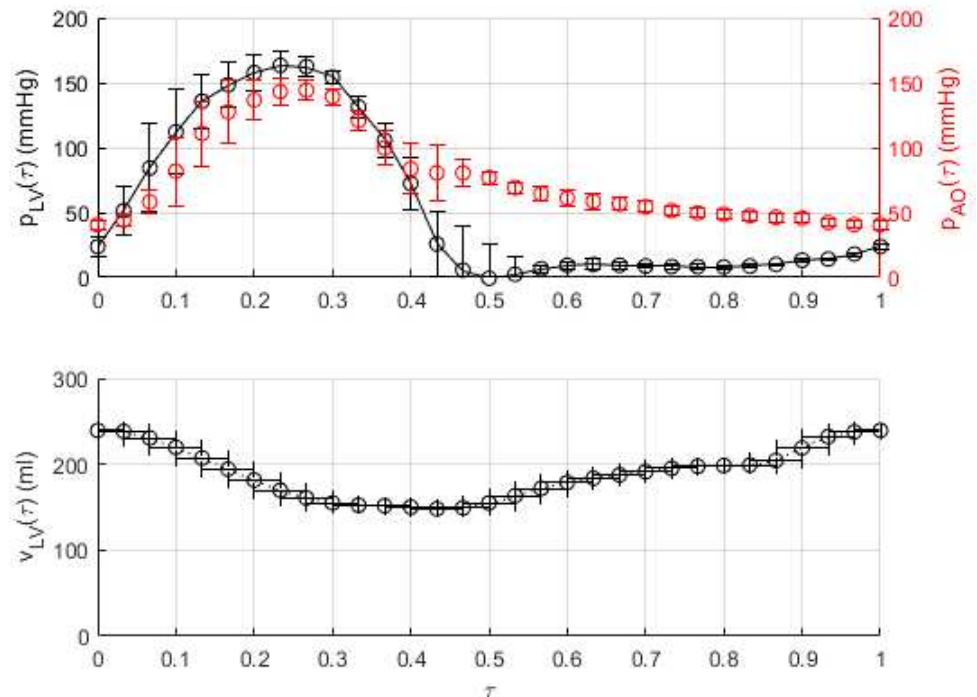


Figure 3. Raw time-series data. Top panel. Downsampled aortic (right ordinate) and left ventricular (left ordinate) pressure variation. These pressure time-series (original sampling rate 120 Hz) were acquired with a concurrent ECG time-series (ECG 1 lead) in the catheterisation laboratory while the patient was undergoing elective PCI. The independent signals were co-registered, using the common background clock of the RR interval of the accompanying ECG 1 recordings. The error bar on these data is derived from the standard deviation of the downsampled pressure time-series sample bins. Bottom panel. LV volume variation. These time-series data are expressed in 30 equispaced CMR phases times. The horizontal error bar corresponds to two CMR phases because the principal source of error in the CMR signals was deemed to originate in the pressure–volume co-registration, which was corrected by a rigid shift, relative to the pressure signals, of about two CMR phases. The data in both panels have time period $\frac{60}{HR}$ secs, but the patient HR and systolic time typically vary between the data collections.

When times T_{ao}^p and T_{ao}^v are not simultaneous, a plausible co-registration is imposed by postulating a shift, or delay in the data $\{v_{LV}(\tau_i), i = 0, \dots, 29\}$ of $\delta_t^{ao} = (T_{ao}^p - T_{ao}^v)$ CMR phases. Similarly, $\delta_t^{mit} = (T_{mit}^p - T_{mit}^v)$ was evaluated. The final rigid shift of CMR volume time-series data is

$$S \approx \frac{(\delta_t^{ao} + \delta_t^{mit})}{2}, \quad S \in \mathbb{N}, \quad 0 \leq S \leq 29.$$

Here, the symbol \approx is used to denote a rounded value. The result of applying the rigid shift defined in Table 7 to our volume time-series data transforms the PV loop; see Figure 4, bottom panel. Our processing paradigm may be summarised as: *constrain the LV pressure and volume time-series to conform to accepted PV loop physiology.*

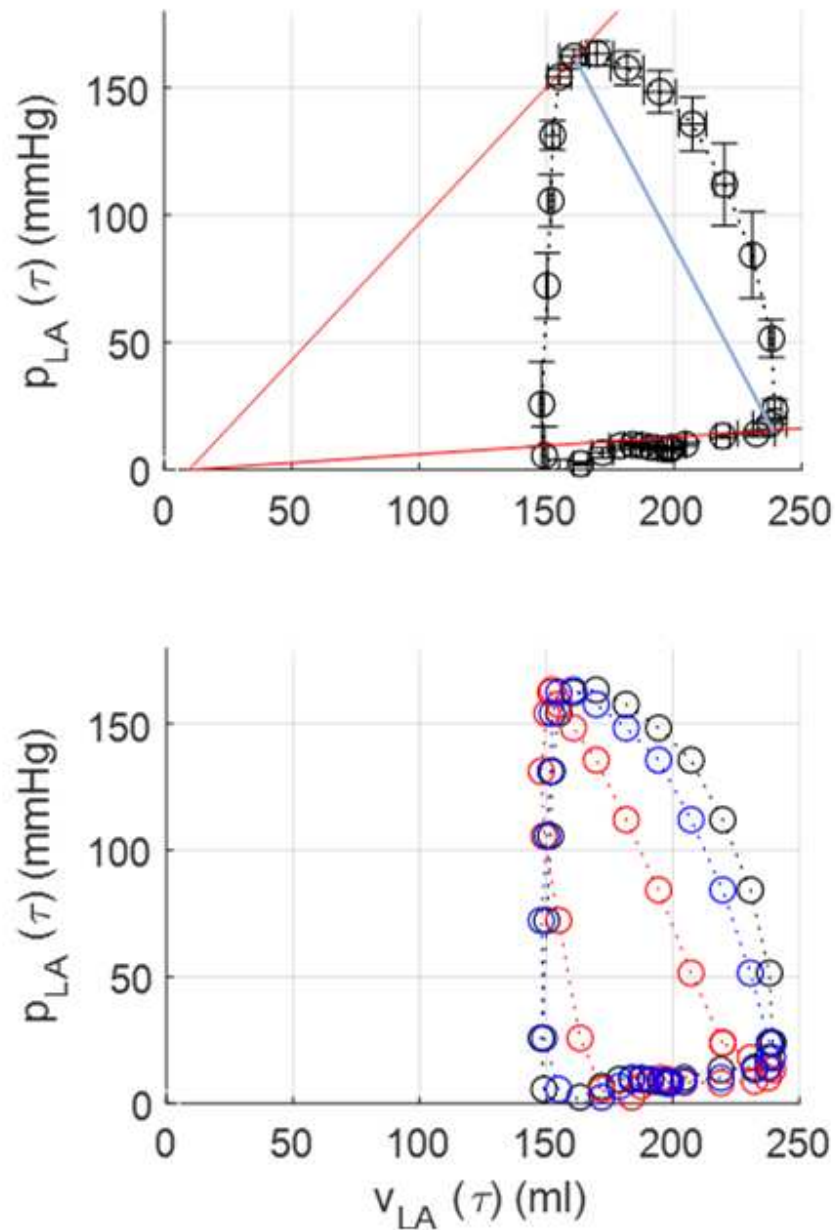


Figure 4. Patient-specific PV loops. Top panel. The closed curve, or loop, derives from the raw data in Figure 3, appropriately co-registered. Ventricular–arterial coupling [20] is measured by the modulus of the gradient of the blue solid line. Isovolumetric compression (right) and relaxation (left) segments are apparent. The volume enclosed within the PV loop is the useful mechanical work, applied to ejected fluid. Wasted work is calculated from the area bounded by the red lines and the left-hand side of the PV loop. Bottom panel. One PV loop based up the same data as shown in the top panel, but using different co-registrations of pressure and volume time-series data. The primitive co-registration (red) has no rigid shift applied to the volume data; the blue dataset shows the result of a rigid shift of one CMR phase, and the black data show the result of a shift of two CMR phases (the value of the shift obtained by synchronising the valve timing points). These data demonstrate the clear need for careful co-registration of the two signals.

With an acceptable co-registration of pressure and volume data, we derive the LV double Hill elastance function parameters. $E_{LV,max}$ (widely termed “contractility”) and $E_{LV,min}$ (“compliance”) are assigned directly

$$E_{LV,max} = \max_i \left(\frac{p_{LV}(t_i)}{v_{LV}(t_i)} \right), \quad E_{LV,min} = \min_i \left(\frac{p_{LV}(t_i)}{v_{LV}(t_i)} \right). \quad (6)$$

Table 7. Identification of mitral and aortic valve opening times, in LV pressure and volume time-series data. Each valve opening instant was identified by multiple criteria (column 3). Discrete time-series data temporal derivatives were evaluated by the class of finite difference approximation stated in column 4. Column 5 defines the notation for the identified cycle time fraction.

Valve	Time-Series	Valve Opening Signature	Difference	Notation
Aortic	pressure	$p_{LV} \gtrsim 80 \text{ mmHg}$ $\max_t \left(\frac{dp_{LV}}{dt} \right)$	central	T_{ao}^p
	volume	$\frac{dv_{LV}}{dt} \lesssim 5 \text{ mL/s}$ close to $\max_t(v_{LV})$	forward	T_{ao}^v
Mitral	pressure	$\frac{dp_{LV}}{dt} < 0$ $\frac{d^2 p_{LV}}{dt^2} \gtrsim 0$	central	T_{mit}^p
	volume	$p_{LV} \approx 10 \text{ mmHg}$ $\left(\frac{dv_{LV}}{dt} \right) > 0$ $\left(\frac{d^2 v_{LV}}{dt^2} \right) > 0$	forward	T_{mit}^v

The remaining activation function parameters accrue by seeking the extremum of a multi-variate function, which is assumed to be differentiable

$$f(n_1, n_2, \tau_1, \tau_2) = \sum_{i=0}^{29} (p_{LV}(\tau_i) - E(\tau_i; \underline{\theta})v_{LV}(\tau_i)), \quad \underline{\theta} = (n_1, n_2, \tau_1, \tau_2)^T \subset \underline{\Theta}. \quad (7)$$

Note, n_1, n_2, τ_1, τ_2 are variables (parameters) on the left (right)-hand side of Equation (7). Minimisation was performed using a gradient descent, initialised to the population average [12]. Figure 5 below shows a derived elastance function.

In this way, our mechanical time-series signals are downsampled onto a common rate of $\frac{60}{30HR}$ Hz, suitably co-registered, and then used to deduce a personalised $E_{LV}(\tau)$ for each patient. These data will be recycled as 0D system model personalisation targets, both as discrete time-series and derived metrics.

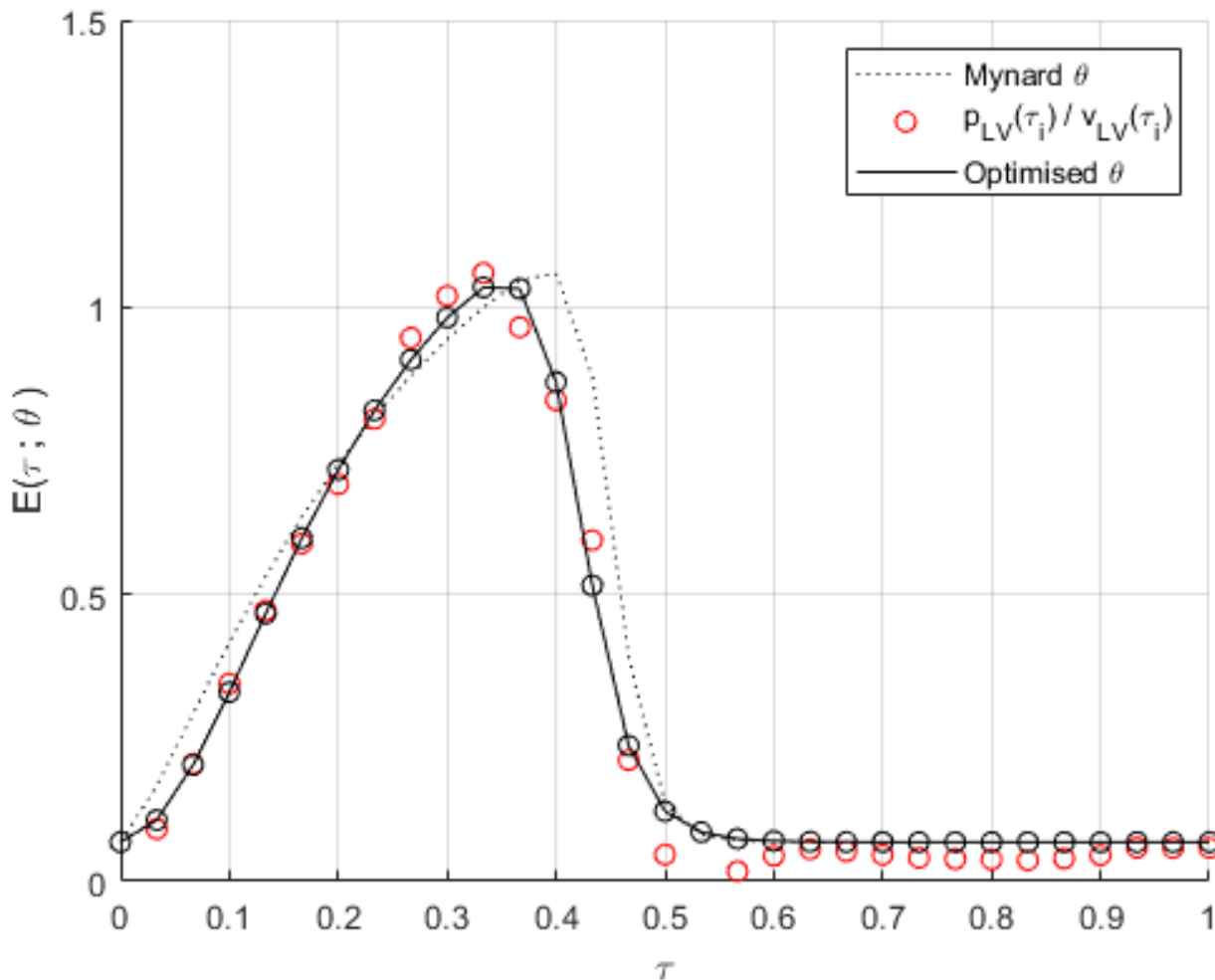


Figure 5. A personalised elastance function. The solid line corresponds to the optimum elastance function, obtained from suitably co-registered coordinates $(p_{LV}(\tau_i), v_{LV}(\tau_i))$, $i = 0, \dots, 29$ using the cost function in Equation (7), minimised using a gradient descent simplex method. Broken line: our common initialisation, using Mynard’s population average [12] parameterisation, θ . Open red circles: raw data, with the appropriate shift applied. Black circles and line: optimised fit on the shifted data minimising the residual declared in Equation (7).

3.2.2. Exercise/Monitoring Data Processing

CAD and cardiorespiratory fitness are linked. Endothelial nitric oxide synthase (eNOS) prevents platelet aggregation and white cell adhesion and inhibits vascular smooth muscle cell proliferation [28], and regular physical exercise enhances bioavailability of eNOS and regeneration of the vascular endothelium [29]. Conversely, inactivity is associated with pathological processes preceding atherosclerosis and CAD [30]. As a result, a dose–response relationship exists between physical activity and the risk of CAD [31], with exercise capacity predictive of mortality, myocardial infarction and risk of re-vascularisation in patients with established CAD [32]; see Figure 6. Assessing patients’ activity and exercise capacity is key in the management and assessment of CAD. For completeness, therefore, we summarise, in two categories, the study exercise and activity data which will, in future work, quantify the change in patient exercise tolerance attending measured PCI-related physiological changes.

1. Home activity monitoring. Fitbit™ Charge 4 wrist watches (Healthy Metrics Research Inc. San Francisco, CA, USA) and a smartphone were used. Data monitoring started at recruitment and extended up to six months post PCI. All data were uploaded

to the Fitbit website simultaneously through a smartphone application and then exported as coarse-grained time-series (mechanical energy consumption, distance walked, minutes spent sedentary, light, fairly, and great activity). Concurrent HR data were also exported as downsampled HR data, which were simultaneously updated throughout the day as time-averaged values every 10–15 min.

2. Formal six-minute walk tests (6MWT). These were performed at baseline before the PCI (ideally one day) with a repeat assessment after three and six months. In these standard clinical assessments, the data collected were cuff blood pressure, HR and distance walked.

We remark that exercise training in CAD is superior to PCI in improving event-free survival and exercise capacity and is at a much lower cost [33], and the total distance walked is a proxy for cumulative CO.

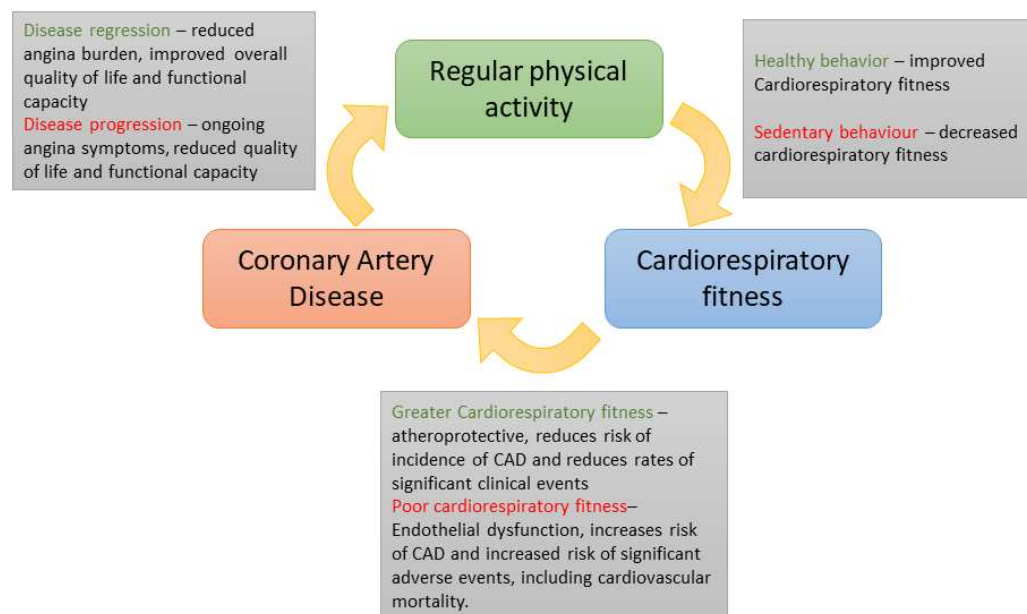


Figure 6. Schematic representation of the relationship between exercise, coronary artery disease progression and cardio-pulmonary fitness and the underlying physiology. The exercise and activity data gathered in this study will eventually expose quantitative links between physical activity, cardio-respiratory fitness and coronary artery disease.

4. Results

Three randomly chosen patients designated A, \dots, C were used to validate our personalisation process, by demonstrating an accurate in silico description of patients’ pre-PCI rest state. Since changes in arterial geometry accompanying re-vascularisation are recorded, PCI-modified MVR and stenotic Bernoulli resistance coefficients will accrue with our approach. Thus, data such as those presented here will eventually be available on the post-operative patient; see Section 5. Results fall into two categories: (i) data on our methodology as summarised in Tables 1 and 4 and (ii) the emergent patient representations.

4.1. Elastance Function Evaluation

Downsampling and ensemble averaging of patient LV and aortic pressure time-series datasets were performed straightforwardly. We proceed to protocol step 2 (a personal $E_{LV}(\tau)$), where we encounter the sensitivity of $E_{LV}(\tau)$, to the co-registration of pressure and volume data. See Table 8 and Figure 7, which describe patient B, who required the largest shift. The PV loop illustrates the importance of co-registration, in Figure 4, where the PV loop shape progressively acquires accepted physiological features of iso-volumetric compression and relaxation phases. The corresponding sensitivity of $E_{LV}(\tau)$, in Figure 7, is quantified by the parameterisations in Table 8. We defer further comment to Section 5.

Figure 8 shows the personalised $E_{LV}(\tau)$ (left) and PV loop (right) for patients A, . . . , C. The elastance data take correctly co-registered LV pressure and volumes and show the initial (red) and optimised (black) fit. The PV loops in the right-hand column show the importance of co-registration case by case, with the PV loop obtained without co-registration shown in red and that with an appropriate co-registration in black.

Table 8. Sensitivity of LV double Hill elastance function parameterisation. For a single patient B, fitted double Hill elastance function shape parameters are declared for a range of co-registration shifts. We deem a shift of 5 in the last column to be the correct co-registration for this particular patient. The corresponding elastance function sequence is plotted in Figure 7.

	Shift	1	2	3	4	5
double Hill LV elastance parameter	n_1	1.91	1.83	1.78	1.68	1.52
	n_2	16.46	17.93	18.06	17.52	17.04
	τ_1	0.28	0.32	0.38	0.47	0.73
	τ_2	0.47	0.48	0.49	0.49	0.49
	$E_{LV,min}$	0.04	0.04	0.04	0.04	0.04
	$E_{LV,max}$	2.95	2.86	2.68	2.48	2.27

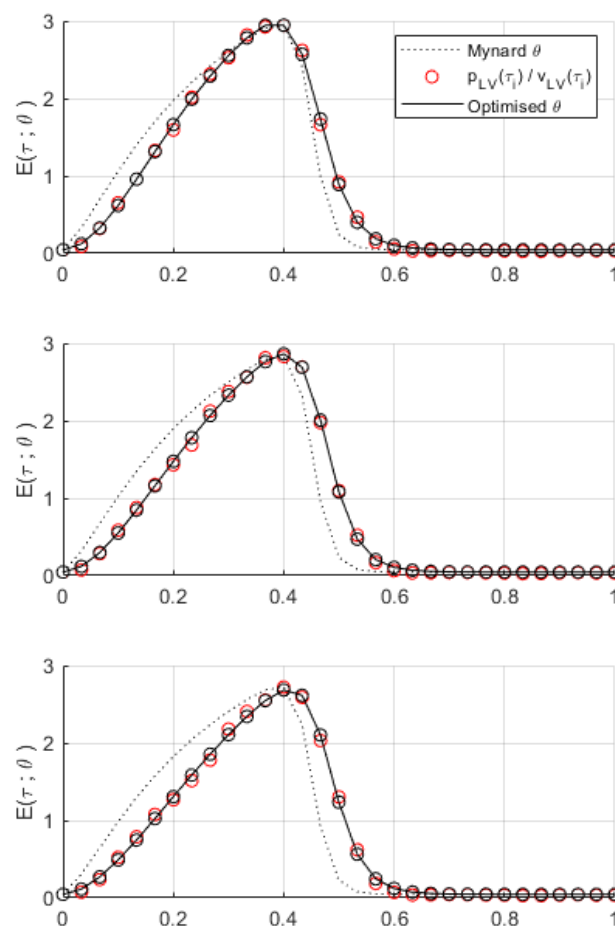


Figure 7. Cont.

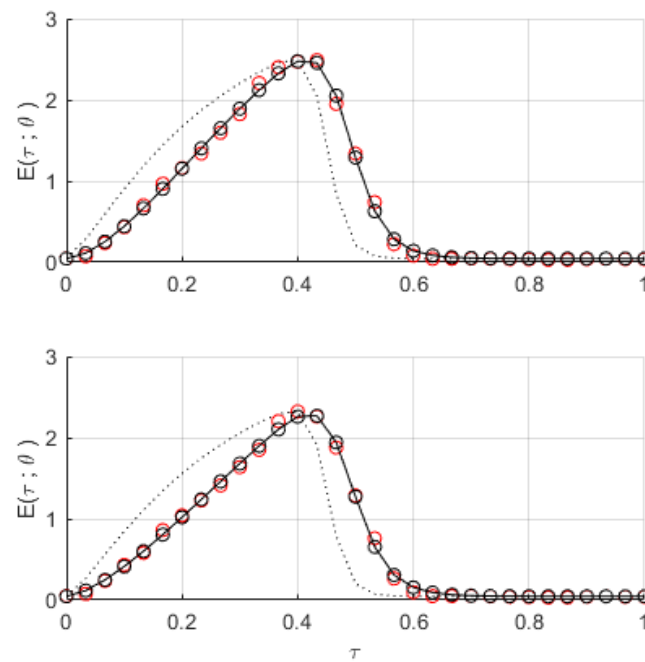


Figure 7. Sensitivity of a patient elastance function to co-registration shift. Data correspond to the double Hill elastance function parameters in Table 8. The shift increases top to bottom with the bottom panel corresponding to the expected shift of 5 phases, deduced using the co-registration declared in Table 9. The broken line shows our common initialisation using Mynard’s population average [12] parameterisation. Open red circles show the raw data with the appropriate shift applied. The black circles and the line show the optimised fit on the shifted data from a gradient descent simplex method applied to Equation (7).

Table 9. Patient-specific LV double Hill elastance function parameters. These parameterisations result from fitting the product $v_{LV}(\tau_i) \times E(\tau_i; \theta)$ to the measured, downsampled pressure $p_{LV}(\tau_i)$, using the cost function defined in Equation (7) and a gradient descent method. The applied co-registration rigid shift, or relative delay, applied to the volume data is declared in the first row.

Patient ID		A	B	C
Co-Registration Rigid Shift		1	5	2
double Hill LV elastance parameter	τ_1	0.29	0.54	0.82
	τ_2	0.42	0.5	0.42
	n_1	1.58	1.56	1.26
	n_2	17.53	17.96	19.95
	$E_{LV,max}$	1.1	2.22	2.17
	$E_{LV,min}$	0.05	0.03	0.03

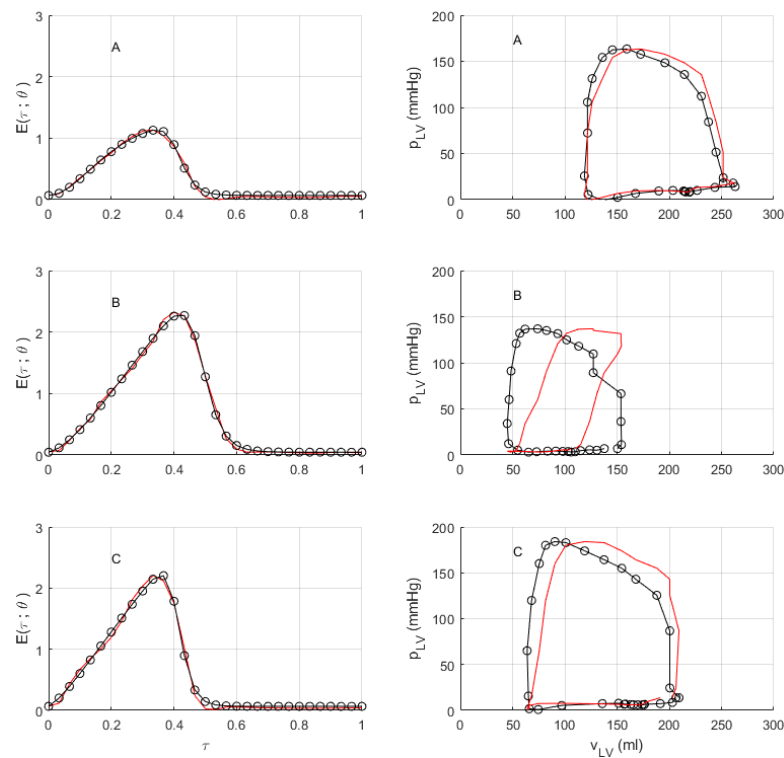


Figure 8. Patient-specific PV loops and elastance functions, for patients A, . . . , C. Left column. Patient-specific elastance functions. Red lines correspond to LV pressure and volume time-series data, which are correctly co-registered according to the criteria declared in Table 7 but which is not optimised. Black circles, with black lines to guide the eye, correspond to an optimised, double Hill elastance function parameterisation, obtained by minimising the residual declared in Equation (7), targeting the 30 downsampled LV pressure time samples, using the 30 LV volume time samples. Right column. The corresponding patient-specific PV loops. These data were processed as described in the text, with the personal co-registration shifts identified in Table 8. The red line shows the result which would be obtained without any co-registration. The black circles, with black lines to guide the eye, are the co-registered data.

4.2. Tuning Protocol Evaluation

Steps 0, 1, and 2 culminate in a personal $E_{LV}(\tau)$ which is input into the system 0D model. The latter then provides time-series outputs for LV and aortic pressures and LV volume at the end of step 3; see Figure 9. The cost function used to acquire these data, Equation (1), equally weights its five targets. Step 3 uses a genetic algorithm (GA) to localise the global cost function minimum, by adjusting the systemic windkessel. In general, the LV diastolic phase exhibits the largest discrepancy between model outputs and targets. This suggests parameters, such as mitral valve resistances and left atrial (LA) elastance, as secondary targets for step 4, which uses a less expensive gradient descent search, on the assumption that previous GA tuning will first have located the correct region. The initial values of the input parameters of the mitral valve Bernoulli resistance and $E_{LA}(\tau)$ are specified in Tables 1 and 5. Step 4 retains the targets of step 3 but adds the LV volume time-series. That step 4 favours the diastolic phase, particularly for cases A and C, is apparent from Figure 9, which shows outputs at the end of step 3 in the left column and outputs from the end of step 4 in the right column.

Having assigned systemic and left-heart energetic parameters, it remains to tune flow in patients’ coronary circulations. The coronaries sequester a small fraction of cardiac output [18]. It is reasonable to suppose that this does not perturb already identified systemic and left heart parameters. The tuning of coronaries in step 5 relies upon CFD data to assign

the MVR and stenotic Bernoulli resistance coefficients. The latter rely on data declared in Tables 10 and 11 and are derived as described in Section 4.3.

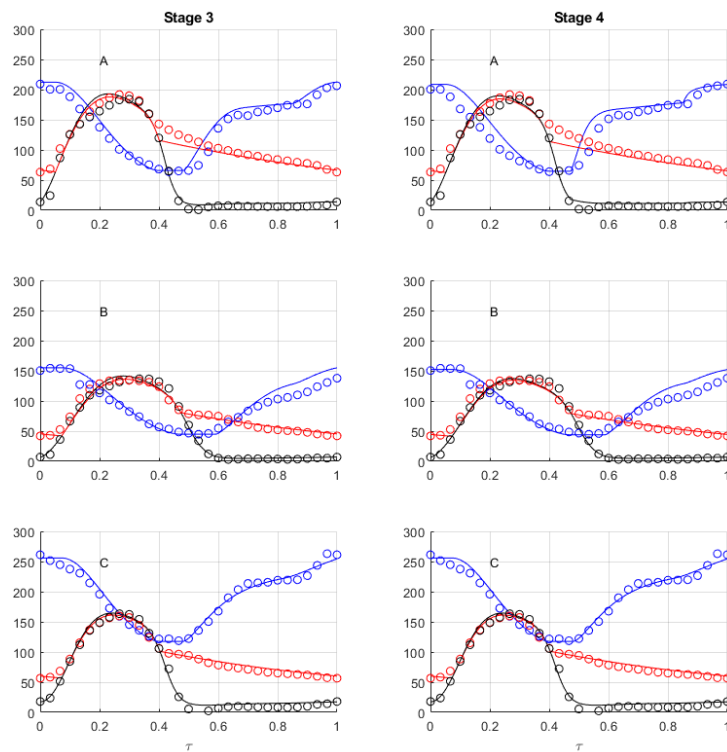


Figure 9. Systemic parameter tuning for patients A, B, C. Key OD system model outputs (solid lines) are shown alongside the corresponding ensemble-averaged and downsampled data (open circles). Black line is LV pressure (mmHg), red line is aortic pressure (mmHg), and blue line is LV volume (mL). All data that were acquired after the appropriate personal elastance function assigned in step 2 had been ingested. Left column, step 3. The search used the GA guided by the cost function in Equation (1), with equal weights applied to patients’ discrete LV pressure and volume extrema and the aortic time-series data. These data result from tuning the following subset of the OD model input parameters $\{L, R_{prox}, C_{prox}, R_{dist}\}$ of the systemic circulation. Right column, step 4. The search used a gradient descent method based on the cost function, Equation (1), with equal weights applied to patients’ discrete LV pressure, volume extrema, aortic time-series data and now LV volume data. These data result from tuning the following subset of the OD model input parameters $\{a_{mit}, b_{mit}, E_{LA,min}, E_{LA,max}, \tau_{1,mit}, \tau_{2,mit}\}$.

4.3. CFD Data Evaluation

Patients’ stenotic Bernoulli resistance coefficients were derived, as discussed above, from VIRTUheart™ (University of Sheffield, Sheffield, UK). VirtuQ™ (University of Sheffield, Sheffield, UK) was used to compute the corresponding MVRs. Both tools assume steady flow. Furthermore, VIRTUheart approximates pressure distal to the MVR as zero. The first assumption is raised within our *transient* OD system model. Moreover, the OD system model, with its four hear chambers, develops an unconstrained pressure distal to the MVR. The stenotic Bernoulli resistance coefficients ingested into the system OD model (Table 10) are deemed to be unaffected by these differences. However, the MVR yielded by our CFD tool requires the correction in Equation (8)

$$MVR \rightarrow \left(\frac{\langle p_d(\tau) \rangle_\tau - \langle p_{RA}(\tau) \rangle_\tau}{\langle p_d(\tau) \rangle_\tau} \right) MVR. \quad (8)$$

Tables 10 and 11 declare the patient-specific CFD data inputted into the system OD model. There, we encounter that sparsity and incompleteness which are typical of clinical

data- none of our selected patients have three vessel disease and others have total coronary occlusion (TCO). The latte precludes all treatment but which can still be mapped to the coronary artery module in Figure 1 however, by setting large stenotic resistance coefficients. The latter are used to determine the pressure drop, δP_* , across a lesion from the flow, using Equation (9)

$$\delta P_* = R_{sten*,a}q_*^2 + R_{sten*,b}q_* \tag{9}$$

Above, * identifies the particular vessel.

Table 10. Coronary artery average pressure data. Time average pressure for lesion-proximal, aortic sinus, and lesion-distal locations. Study data are recorded for treated arteries only. Pressures were obtained using a pressure transducer by catheterisation during the PCI process.

Patient	Vessel					
	LAD		LCx		RCA	
	P_{prox}	P_{dist}	P_{prox}	P_{dist}	P_{prox}	P_{dist}
UNIT	mmHg	mmHg	mmHg	mmHg	mmHg	mmHg
A	88.60	74.50	~	~	~	~
B	103.71	99.17	103.95	101.69	~	~
C	121.74	115.73	~	~	127.23	125.89

Table 11. CFD-derived data for the patient coronary arteries. Stenotic Bernoulli resistance coefficients and MVRs for patients A,B,C.

Patient	Metric	Unit	Vessel		
			LAD	LCx	RCA
A	MVR	mmHg·s/mL	1.50	~	~
	$R_{sten,a}$	mmHg·s ² /mL ²	28.45	~	~
	$R_{sten,b}$	mmHg·s/mL	28.58	~	~
B	MVR	mmHg·s/mL	0.77	1.10	~
	$R_{sten,a}$	mmHg·s ² /mL ²	16.56	10.22	~
	$R_{sten,b}$	mmHg·s/mL	22.34	14.33	~
C	MVR	mmHg·s/mL	1.75	~	1.01
	$R_{sten,a}$	mmHg·s ² /mL ²	22.34	~	16.67
	$R_{sten,b}$	mmHg·s/mL	12.33	~	14.11

5. Discussion

We have characterised the pre-PCI patient state, but equivalent data exist for post-PCI patient states; thus, the approach described here may be used to examine post-intervention physiology. Our methodology brings within scope for the first time, a means to relate qualitative changes in physiology to changes in, e.g., exercise tolerance. The importance of a careful co-registration of our LV pressure and volume time-series data is underscored by the data in Figure 7 and the corresponding double Hill parameterisations, declared in Table 8. These data show LV contractility ($E_{LV,max}$) and systolic activation function parameters τ_1, n_1 to be the most sensitive elastance parameters to co-registration shift. These parameters respectively quantify LV contractility and the vigour of systolic onset and are very important indicators of cardiac health.

Step 2 of our protocol is seen to be robust and necessary. It represents a successful means of dealing with nonsimultaneous pressure and volume time-series data. From the data of Figure 8, it is apparent that a range of elastance functions and PV loops are successfully addressed. The change in the elastance function as correct co-registration is progressively applied demonstrates a significant degree of sensitivity in the elastance

function. This underscores the importance of step 2 in our protocol. From Figure 8, it is also apparent that the PV loop of some cases is rather more sensitive than others to our rigid shift co-registration of pressure and volume time-series data.

From Figure 8, we see that the optimisation process enshrined in Equation (7) makes relatively little difference to the final shape of the elastance function, certainly compared with that produced by the volume and pressure time-series co-registrations.

6. Conclusions

We have verified the ability of appropriate protocols, PCI-acquired data and a suitable 0D system model, robustly interacting with 3D CFD models to recover a quantitative *in silico* representation of three individual patients' physiological and pre-PCI cardiovascular state. This depiction relies on parsing diverse clinical data, compiled during the elective PCI clinical pathway. Specifically, our hierarchical, multi-stage protocol is shown to identify prioritised input model parameters of cardiac energetics and coronary perfusion, within a 0D (compartmental) four-chamber system model with data-adapted coronary artery topology. Using this, we reached verifiable *in silico* representations of significant LV aortic and coronary artery volume, flow and pressure time-series. This process of input parameter identification is known in the clinical context as model personalisation. It is a key determinant of clinical utility, which urges a parsimonious model or (as here) the prioritisation of a subset of model input parameters, chosen with the supporting sensitivity and orthogonality analysis, provided in the appendices. The present study requires accurate representation of coronary flow states which are dominated by diastolic dynamics. The coupling of the coronary arteries' compliances (capacitances) to the appropriate chamber pressure (see Figure 1) apparently recovers diastolic dominance in coronary flow.

Time-series data play a defining role. To utilise them optimally, it was necessary to reconcile data collected at different stages of the clinical pathway with patients at different points in their physiological envelopes. This is deemed to be our largest source of error. The time-series data in question are non-invasive left ventricular volume, derived from CMR, and invasive LV and aortic pressures measured during PCI. Our approach involves downsampling pressure to accord with MRI phases and devising a suitable rigid phase shift, based upon LV valve timings, to overcome an identified co-registration error; results were assessed by the qualitative credibility of a physiological properties inferred from the LV PV loop. The commensurate LV elastance function is an input into the system 0D model personalisation process. It is shown to be sensitive to the co-registration of time-series data. Possibly, the most consequential, purely clinical outcome of this work is that we have been able to obtain credible results for patient PV loops and left-ventricular elastance functions by using a straightforward co-registration of non-simultaneous invasive pressure and non-invasive volume data when guided by rudimentary and therefore robust physiological principles.

Despite sources of error, it is apparent that there remains sufficient depth in the clinical pathway dataset to build appropriate digital twins, and we present as evidence data for three patients in the pre-PCI state. A route to the complementary, post-intervention description of the patient now lies open. One simply needs to apply the current workflow to extant data which are of equivalent form to that considered here. Therefore, using our methodology, one can expect to develop both pre- and post-PCI representation of patients from which to measure physiological changes attending PCI. Section 3.2.2 outlines a range of relevant activity measures which might be used meaningfully to contextualise this change in global ischaemic burden. Put another way, the act of correlating these model-derived statistics of the study data has the potential to reveal relationships between coronary physiology, cardiac energetics and physical activity, as well as providing clinical decision support. The model represents a means not only to establish a connection between global coronary perfusion and cardiac energetics, but to quantify it.

Author Contributions: A.A.B. and G.W., P.G. collected, curated and prepared all data. D.R.H., D.R. and F.v.d.V. devised the original model elements. K.C., A.L., I.H., A.J.N., M.M., F.v.d.V. and D.R.H. devised, implemented and adapted the model elements and designed the data-handling protocols. Clinicians P.D.M., R.C.G., P.G. and J.P.G. performed the PCI interventions from which all data are harvested. J.P.G. designed and led the study. All authors have read and agreed to the published version of the manuscript.

Funding: This publication is supported by the European Union’s Horizon 2020 research and innovation programme under grant agreement Sano No. 857533 and by the Sano project carried out within the International Research Agendas Programme of the Foundation for Polish Science, co-financed by the European Union under the European Regional Development Fund.

Institutional Review Board Statement: The study was conducted in accordance with the Declaration of Helsinki, and approved by the UK’s NHS Health Research Authority, sponsored by Sheffield Teaching Hospitals NHS Foundation Trust, (IRAS project ID 272069, REC reference 20/NS/0063, approved 23 March 2020).

Informed Consent Statement: Informed consent was obtained from all subjects involved in the study. Written informed consent has been obtained from the patients to publish this paper.

Data Availability Statement: Study data are not publicly available due to ethical restrictions, which apply to personal patient data. The data presented in this study are available on request from the corresponding author, Ian Halliday.

Conflicts of Interest: There are no conflict of interest.

Appendix A. System Model

Appendix A.1. System Model Dynamical Equations

It is possible to formulate the 0D model in terms of ordinary differential equations or differential algebraic equations [23]. Compartments are specified by their time-dependant dynamic pressure p (mmHg), inlet flow q (mL/s) and volume v (mL). The equations relating to the passive compartmental state variables all take the form

$$\frac{dv_i}{dt} = q_i - q_{i+1}, \quad \frac{dp_i}{dt} = \frac{1}{C_i}(q_i - q_{i+1}), \quad q_i = \frac{p_i - p_{i+1}}{R_i}. \quad (A1)$$

Above, the subscripts $(i - 1), i, (i + 1)$ respectively represent the proximal, present and distal system compartments, v_i (mL) denotes the circulating (stressed) volume and C_i (mL/mmHg) and R_i (mmHg/s/mL) denote compartmental compliance and the Ohmic, or Bernoulli, resistance between compartments $i, (i + 1)$. We turn to the active system compartments, described by so-called activation functions, and valve characteristics.

Appendix A.2. Sub-Models—Chamber Elastances and Valve Characteristic Functions

The double Hill elastance used here [12,14] is that in most widespread use within the clinical and physiological communities. The same essential model is used to express the biomechanics of all four heart chambers. Shi proposed an alternative model, with more compact support, which is arguably more intuitive [34], having similar properties. Neither takes into account stress stiffening in systole. Arts et al. [35] and Bovendeerd et al. [36] developed a model based on a more formal approach which accounts for stress-stiffening of the chamber. The double Hill function for it is expressed in terms of an activation or shape function, which is a product of monotonically increasing and decreasing expressions, as follows:

$$e(\tau; n_1, n_2, \tau_1, \tau_2) = \frac{x}{(1+x)(1+y)}, \quad x = \left(\frac{\tau}{\tau_1}\right)^{n_1}, \quad y = \left(\frac{\tau}{\tau_2}\right)^{n_2}.$$

A model elastance is then assigned

$$E(\tau; \theta) = E_{max} \left(\frac{e(\tau; n_1, n_2, \tau_1, \tau_2)}{\max_{\tau}(e(\tau; n_1, n_2, \tau_1, \tau_2))} \right) + E_{min}.$$

Above, $\underline{\theta}$ denotes the set elastance parameters $\{E_{max}, E_{min}, n_1, n_2, \tau_1, \tau_2\}$. E_{max} and E_{min} specify chamber contractility and compliance, respectively. Parameter n_2 (the relaxation rate constant) is commonly set to large values to produce a sharp cut-off in $E(\tau; \underline{\theta})$ at the systolic to diastolic boundary. The double Hill parameter, τ_2 , (the diastolic time constant) is the principal determinant of the systolic to diastolic ratio. Amplitude and shape parameters differ between all four chambers. Moreover, atrial elastance functions have adjustable phase, relative to ventricular elastances.

Valve characteristic functions express the relationship between flow through a valve, Q_{valve} , and pressure difference, δp , between separated compartments. Valves used in this work are diodes, having quadratic (Bernoulli) flow-pressure characteristics under forward bias with no leakage flow under reverse bias

$$q_*(\tau) = \begin{cases} a_{1,*}\delta p(\tau)^2 + a_{2,*}\delta p(\tau) & \delta p(\tau) > 0, \\ 0 & \delta p(\tau) \leq 0. \end{cases}$$

Above, the free subscript $*$ denotes one of our four valve flows.

Appendix B. Sensitivity and Orthogonality Analysis

Personalisation is a parameter identifiability analysis [5] applied to a chosen subset of input parameters which are often hypothesised to serve as clinical biomarkers and to a set of output metrics which correspond to available clinical data. The foundations of input parameter identifiability are sensitivity and input parameter orthogonality analysis. Using such, one can turn to formal methods (see, e.g., Li et al. [37]) which help to determine subsets of model input parameters which are optimal for personalisation [38]. Relative sensitivity and input parameter orthogonality analyses, derived from the operation of our system 0D model, are presented here in two forms. First, we consider an full analysis, based on the whole set of our system model’s input parameters with an impractically large range of discrete outputs. Then we present the same analyses, with the list of input parameters restricted, to reflect those which we use in our patient personalisation process. For this subset, we also restrict the range of discrete model outputs to be representative of our study’s patient data.

The relative sensitivity of the m th discrete output, X_m , on the n th discrete input, θ_n , is measured by a numerical approximation to the normalised partial derivative

$$S_{nm} = \frac{\theta_{n,0}}{X_m(\underline{\Theta}_0)} \left[\frac{\partial X_m}{\partial \theta_n} \right]_{\underline{\Theta}_0}, \quad 1 \leq m \leq M, \quad 1 \leq n \leq N. \tag{A2}$$

Above, the model base state, $\underline{\Theta}_0$, corresponds to our normal patient, where N (M) is the number of model inputs (outputs) and S_{nm} is a sensitivity matrix element. Noting the system input index, n , which identifies rows of S , we define a relative sensitivity row vector, characteristic of the n th input

$$\underline{s}_n = (S_{n1}, S_{n2}, \dots, S_{nM}), \quad 1 \leq n \leq N. \tag{A3}$$

From such sensitivity vectors, it is possible to measure the linear independence of the action across all outputs, of two chosen input parameters using a simple, intuitive orthogonality measure, which is a straightforward generalisation of the scalar product of two vectors

$$d_{nn'} = \sin \left(\cos^{-1} \left(\frac{\underline{s}_n \cdot \underline{s}_{n'}}{\sqrt{\underline{s}_n \cdot \underline{s}_n} \sqrt{\underline{s}_{n'} \cdot \underline{s}_{n'}}} \right) \right), \quad 1 \leq n, n' \leq N. \tag{A4}$$

Above, for two input parameters having identical action on all outputs, we find $d_{nn'} = 0$. Put another way, if $d_{nn'} = 0$, then incrementing θ_n and $\theta_{n'}$ will move all the system outputs in the same direction. Under such circumstances, while θ_n and $\theta_{n'}$ might each have considerable influence, they do not act upon them differentially. Optimal choices

of input parameters for personalisation should clearly be chosen on the basis of influence and orthogonality. Clearly, $d_{nm} = d_{n'm'}$, and it is convenient to survey the orthogonality of the model input parameters by presenting the square, symmetric matrix d , as a heatmap.

Figure A1 shows the full sensitivity matrix, based upon all inputs and a large range of discrete outputs. Of course, no practical study, however extensive, will have access to the range of outputs shown here. For the sake of completeness, however, we also present the corresponding input parameter orthogonality matrix and the statistics of that dataset in Figures A2 and A3, respectively. These figures are to be interpreted using Table A1.

Of much greater practical significance, certainly for the present study, is the partial sensitivity matrix, now based upon that subset of model inputs which are considered in this study alongside a set of outputs which are representative of the data we access. These data are presented in Figures A4–A6. They suggest that the systemic circulation parameters influence coronary flow. This, of course, is consistent with our assumptions: the recognised principal determinant of LV afterload is the systemic arterial windkessel parameterisation and a reduction in (say) systemic vascular resistance will increase flow to the system, and thereby, the fixed fraction which is sequestered to the coronaries increases. Conversely, changes in the parameterisation of the coronaries have little effect on the systemic metrics. The block diagonal structure in Figure A6 reinforces the conclusion that there is only weak coupling between the coronaries and the systemic and cardiac parameters of our model.

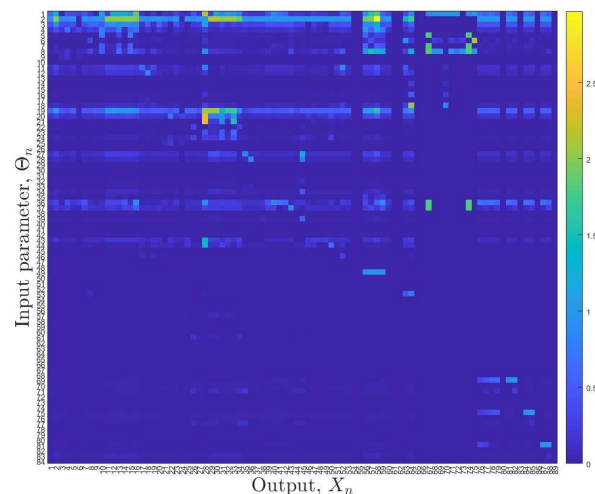


Figure A1. Full relative sensitivity matrix of the model, at base state. The sensitivity matrix is represented here as a heatmap. These data represent the fullest assessment of the studied four-chamber model and are presented for the sake of completeness. Input parameters and outputs are identified by their numerical subscripts, identified in Table A1. Many of the sensitivities are of restricted utility as they are based upon unobservable outputs. A restricted sensitivity analysis is presented in Figure A4 where the range of model inputs and outputs is restricted, in line with data available in the present study. Here, and in a majority of complex models, the heatmap is dominated by a few large sensitivities.

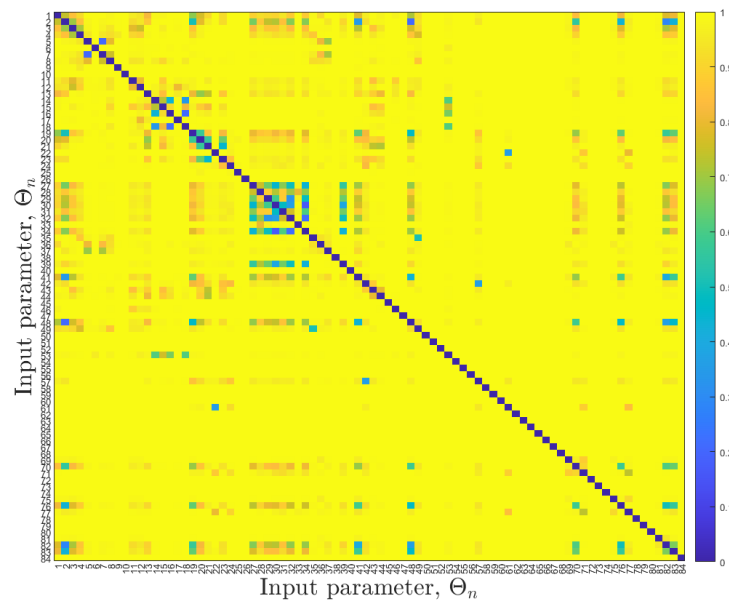


Figure A2. Full input parameter orthogonality analysis of the model sensitivity vectors. This heatmap is a representation of the matrix d (Equation (A4)). Input parameters are identified by their numerical subscripts identified in Table A1. Data are based upon sensitivity vectors, derived from the full model sensitivity matrix, in Figure A1. A more meaningful input parameter orthogonality analysis is presented in Figure A4, where the range of model inputs and outputs is restricted, in line with the data available in the present study.

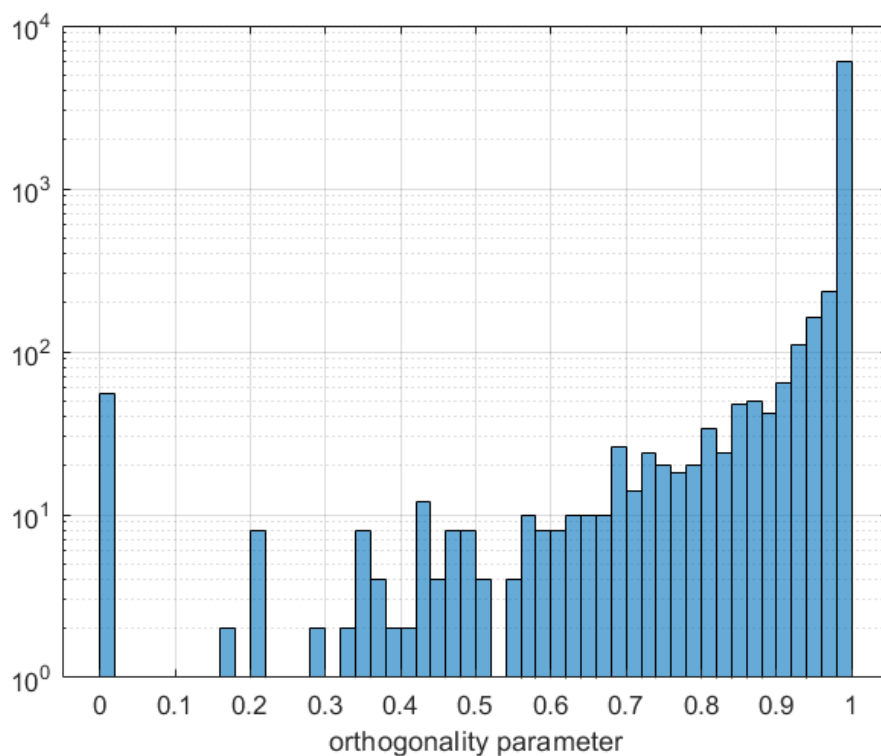


Figure A3. Statistics of the full input parameter orthogonality analysis. The statistical distribution of the matrix elements d_{nm} are shown in heatmap form in Figure A2. The distribution of these data tends to suggest that with a comprehensive set of outputs, a majority of model input parameters are identifiable.

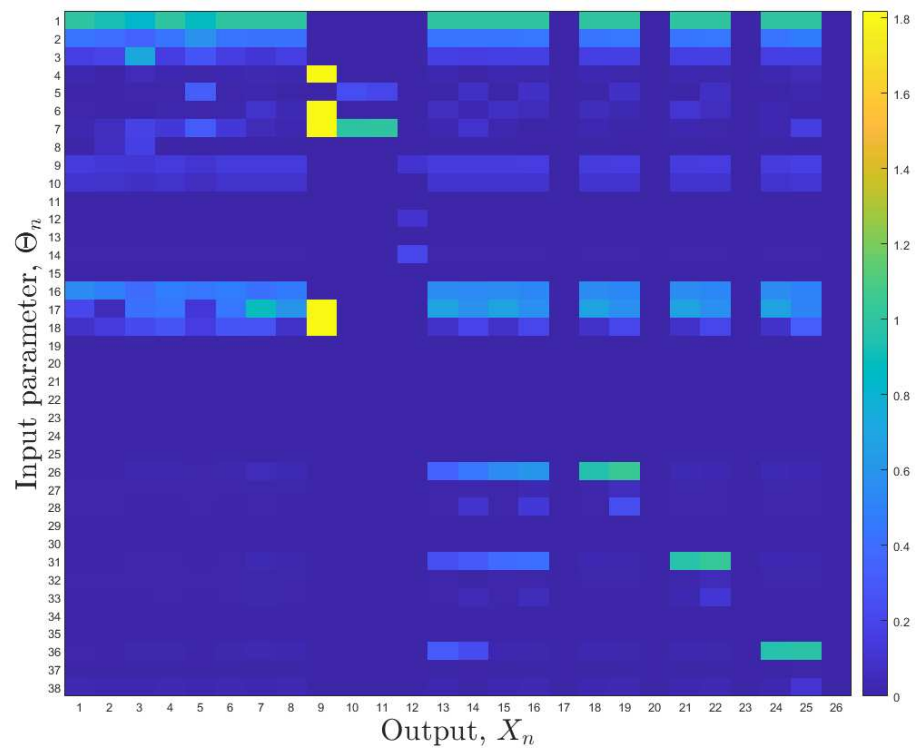


Figure A4. Restricted relative sensitivity matrix of the model, at base state. Relative to the data in Figure A1, here we show the sensitivity matrix based upon model input parameters which are emphasised within this study, combined with outputs which are acquired within the patient clinical pathway. Input parameters and outputs are identified by the numerical subscripts identified in Table A1.

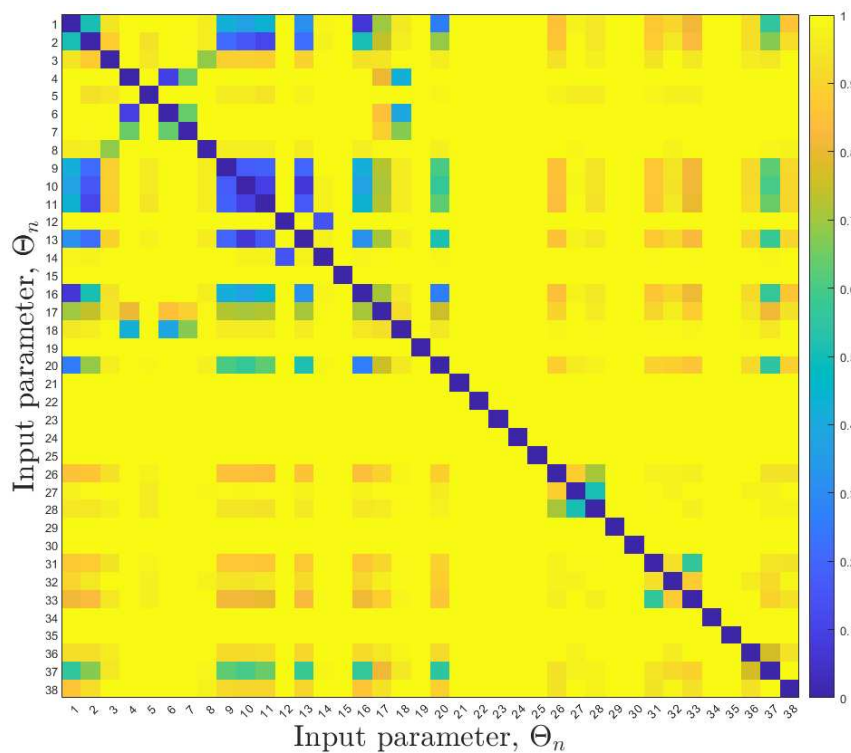


Figure A5. Restricted input parameter orthogonality analysis. These data represent the subset of model input parameters used in this study. The output parameters which are embedded in these data are those effectively declared in the data of figure A4. Input parameters are identified by the subscripts declared in Table A1.

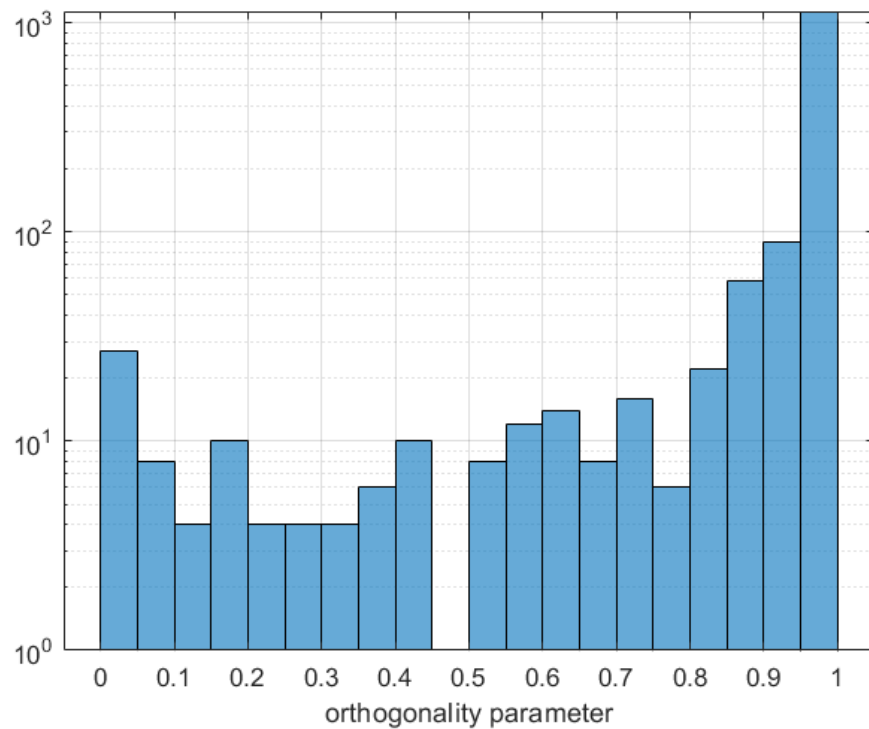


Figure A6. Statistics of the restricted input parameter orthogonality analysis. The statistical distribution of the matrix elements d_{nm} are shown in heatmap form in Figure A5.

Table A1. Key to full and restricted sensitivity and orthogonality analyses in Figures A1, A2, A4 and A5. First column, index, and second and third columns are restricted analysis, fourth and fifth columns are full analysis. Θ_n denotes an input parameter; X_n denotes an output parameter.

n	Θ_n	X_n	Θ_n	X_n
1	Heart Rate	Cardiac Output	Heart Rate	Cardiac Output
2	Mean circ. filling press.	LV End Diastolic Volume	Mean circ. filling press.	Useful Cardiac Power
3	ELVmin	LV End Systolic Volume	ELVmin	LV End Diastolic Volume
4	ELVmax	LV Maximum Pressure	ELVmax	LV End Systolic Volume
5	n1LV	LV Minimum Pressure	n1LV	LV Stroke Volume
6	n2LV	Systemic Artery Systolic Press.	n2LV	LV Ejection Fraction
7	Tau1fLV	Systemic Artery Diastolic Pres.	Tau1fLV	LV Maximum Pressure
8	Tau2fLV	Systemic Artery True MAP	Tau2fLV	LV Minimum Pressure
9	LV fractional time shift	AV Opens	LV volume offset	LV End Diastolic Pressure
10	ELAmin	AV Closes	LV fractional time shift	LV dp/dt (peak)
11	ELAmax	MV Opens	ELAmin	LV Stroke Work per Beat
12	n1LA	MV Closes	ELAmax	LV Stroke Power (Mean)
13	n2LA	Mean Coronary Flow	n1LA	LV Stroke Power (Peak)
14	Tau1fLA	Maximum Coronary Flow	n2LA	LV Myocardial Power (mean)
15	Tau2fLA	Left Main Flow (mean)	Tau1fLA	LV Myocardial Power (peak)
16	LA fractional time shift	Left Main Flow (peak)	Tau2fLA	LV Wasted Myocardial Power (Suga)
17	Systemic Resistance (Prox.)	Left Main 'FFR' (<Pd> / <Pa>)	LA volume offset	LA Maximum Volume
18	Systemic Resistance Distal	Cx Flow (mean)	LA fractional time shift	LA Minimum Volume
19	Systemic Art. Cap (Prox.)	Cx Flow (peak)	ERVmin	LA Maximum Pressure

Table A1. *Cont.*

n	Θ_n	X_n	Θ_n	X_n
20	Systemic Art. Inertance (Prox.)	Cx 'FFR' (<Pd> / <Pa>)	ERVmax	LA Minimum Pressure
21	Mitral Valve quadratic coeff.	LAD Flow (mean)	n1RV	RV End Diastolic Volume
22	Mitral Valve linear coeff.	LAD Flow (peak)	n2RV	RV End Systolic Volume
23	Left main, quadratic coeff.	LAD 'FFR' (<Pd>/<Pa>)	Tau1fRV	RV Stroke Volume
24	Left main, linear coeff.	RCA Flow (mean)	Tau2fRV	RV Ejection Fraction
25	Cx, quadratic coeff.	RCA Flow (peak)	RV volume offset	RV Maximum Pressure
26	Cx, linear coeff.	RCA 'FFR' (<Pd> / <Pa>)	RV fractional time shift	RV Minimum Pressure
27	Cx, RCR total res.	~	ERAMin	RV End Diastolic Pressure
28	Cx, RCR cap.	~	ERAMax	RV dp/dt (peak)
29	Cx Cap. back press. fraction	~	n1RA	RV Stroke Work per Beat
30	LAD, quadratic coeff.	~	n2RA	RV Stroke Power Expenditure
31	LAD, linear coeff.	~	Tau1fRA	RV Stroke Power (Peak)
32	LAD, RCR total resistance	~	Tau2fRA	RV Myocardial Power (mean)
33	LAD, RCR cap,	~	RA volume offset	RV Myocardial Power (peak)
34	LAD Cap. back press. fraction	~	RA fractional time shift	RV Wasted Myocardial Power (Suga)
35	RCA, quadratic coeff.	~	Systemic Resistance Prox.	RA End Diastolic Volume
36	RCA, linear coeff.	~	Systemic Resistance Dist.	RA End Systolic Volume
37	RCA, RCR total resistance	~	Systemic Arterial Prox. Cap.	RA Maximum Pressure
38	RCA, RCR capacitance	~	Systemic Arterial Prox. Unstressed Vol.	RA Minimum Pressure
39	~	~	Systemic Arterial Distal Cap.	Systemic Artery Systolic Pressure
40	~	~	Systemic Arterial Distal Unstressed Vol.	Systemic Artery Diastolic Pressure
41	~	~	Systemic Arterial Inertance (Prox.l)	Systemic Artery Nominal MAP
42	~	~	Pulmonary Resistance Prox.	Systemic Artery True MAP
43	~	~	Pulmonary Resistance Distal	Systemic Artery Pulse Pressure
44	~	~	Pulmonary Arterial Proximal Cap.	Systemic Vein Mean Pressure
45	~	~	Pul. Art. Prox. Unstressed Vol.	Systemic Vein Pulse Pressure
46	~	~	Pul. Art. Distal Cap.	Pulmonary Artery Systolic Pressure
47	~	~	Pulmonary Arterial Distal Unstressed Vol.	Pulmonary Artery Diastolic Pressure
48	~	~	Pulmonary Arterial Inertance (Prox.)	Pulmonary Artery Nominal MAP
49	~	~	Aortic Valve quadratic coeff.	Pulmonary Artery True MAP
50	~	~	Aortic Valve linear coeff.	Pulmonary Artery Pulse Pressure
51	~	~	Aortic Valve regurgitant quadratic coeff.	Pulmonary Vein Mean Pressure
52	~	~	Aortic Valve regurgitant linear coeff.	Pulmonary Vein Pulse Pressure
53	~	~	Mitral Valve quadratic coeff.	AV Forward Flow [ml/beat]
54	~	~	Mitral Valve linear coeff.	AV Regurgitation [ml/beat]
55	~	~	Mitral Valve regurgitant quadratic coeff.	AV Regurgitant Fraction [-]
56	~	~	Mitral Valve regurgitant linear coeff.	AV Maximum Pressure Drop

Table A1. *Cont.*

n	Θ_n	X_n	Θ_n	X_n
57	~	~	Pulmonary Valve quadratic coeff.	AV Mean Pressure Drop
58	~	~	Pulmonary Valve linear coeff.	(Stroke Power Lost):(AV Resistance)
59	~	~	Pulmonary Valve regurgitant quad. coeff.	(Stroke Power Lost):(AV Resistance)
60	~	~	Pulmonary Valve regurgitant linear coeff.	MV Forward Flow [ml/beat]
61	~	~	Tricuspid Valve quadratic coeff.	MV Regurgitation [ml/beat]
62	~	~	Tricuspid Valve linear coeff.	MV Regurgitant Fraction [-]
63	~	~	Tricuspid Valve regurgitant quad. coeff.	MV Maximum Pressure Drop
64	~	~	Tricuspid Valve regurgitant linear coeff.	MV Mean Pressure Drop
65	~	~	Left main, quadratic coeff.	Stroke Power Lost to MV Regurgitation
66	~	~	Left main, linear coeff.	(Stroke Power Lost):(MV Regurgitation)
67	~	~	Cx. quad. coefficient	AV Opens
68	~	~	Cx. linear coefficient	AV Closes
69	~	~	Cx. RCR total resistance	MV Opens
70	~	~	Cx. RCR cap.	MV Closes
71	~	~	Cx. RCR fraction proximal resistance	Period of Systole
72	~	~	Cx. cap. back pressure fraction	Period of Diastole
73	~	~	LAD, quadratic coefficient	Proportion of Heart Period in Systole
74	~	~	LAD, linear coefficient	Period of Isovolumetric Contraction
75	~	~	LAD, RCR total resistance	Period of Isovolumetric Relaxation
76	~	~	LAD, RCR capacitance	Mean Coronary Flow
77	~	~	LAD, RCR fraction proximal resistance	Maximum Coronary Flow
78	~	~	LAD cap. back pressure fraction	Left Main Flow (mean)
79	~	~	RCA, quadratic coefficient	Left Main Flow (peak)
80	~	~	RCA, linear coefficient	Left Main 'FFR' (<Pd> / <Pa>)
81	~	~	RCA, RCR total resistance	Circumflex Flow (mean)
82	~	~	RCA, RCR capacitance	Circumflex Flow (peak)
83	~	~	RCA, RCR fraction proximal resistance	Circumflex 'FFR' (<Pd> / <Pa>)
84	~	~	LAD cap, back pressure fraction	LAD Flow (mean)
85	~	~	~	LAD Flow (peak)
86	~	~	~	LAD 'FFR' (<Pd> / <Pa>)
87	~	~	~	RCA Flow (mean)
88	~	~	~	RCA Flow (peak)
88	~	~	~	RCA 'FFR' (<Pd> / <Pa>)

References

- Shi, Y.; Lawford, P.; Hose, D.R, Review of Zero-D and 1-D Models of Blood Flow in the Cardiovascular System. *BioMed. Eng.* **2011**, *10*, 33. [[CrossRef](#)] [[PubMed](#)]
- Hose, D.R.; Lawford, P.V.; Huberts, W.; Hellevik, L.R.; Omholt, S.; van de Vosse, W. Cardiovascular models for personalised medicine: Where now and where next? *Med. Eng. Phys.* **2019**, *72*, 38. [[CrossRef](#)] [[PubMed](#)]
- Shi, Y. *Lumped-Parameter Cardiovascular Model with Windkessel Afterload*; CellML: Auckland, New Zealand, 2007. Available online: <http://models.cellml.org/exposure/ea64608ab564ee085bef7cde3ed1731e> (accessed on 1 May 2023).
- Korakianitis, T.; Shi, Y. A concentrated parameter model for the human cardiovascular system including heart valve dynamics and atrioventricular interaction. *Med. Eng. Phys.* **2006**, *28*, 613–628. [[CrossRef](#)]
- Saltelli, A.; Ratto, M.; Andres, T.; Campolongo, F.; Cariboni, J.; Gatelli, D.; Saisana, M.; Tarantole, S. *Global Sensitivity Analysis: The Primer*; John Wiley and Sons: Hoboken, NJ, USA, 2008.

6. Morris, P.D.; Ryan, D.; Morton, A.C.; Lycett, R.; Lawford, P.V.; Hose, D.R.; Gunn, J.P. Virtual Fractional Flow Reserve From Coronary Angiography: Modeling the Significance of Coronary Lesions: Results From the VIRTU-1 (VIRTUAL Fractional Flow Reserve From Coronary Angiography). *JACC Cardiovasc. Interv.* **2013**, *6*, 149–157. [[CrossRef](#)]
7. Morris, P.D.; Gosling, R.; Zwierzak, I.; Evans, H.; Aubiniere-Robb, L.; Czechowicz, K.; Evans, P.C.; Hose, D.R.; Lawford, P.V.; Narracott, A.J. A novel method for measuring absolute coronary blood flow and microvascular resistance in patients with ischaemic heart disease. *Cardiovasc. Res.* **2021**, *117*, 1567–1577. [[CrossRef](#)] [[PubMed](#)]
8. Succi, S. *The Lattice Boltzmann Equation for Fluid Dynamics and Beyond*; Clarendon Press: Oxford, UK, 2001.
9. Groen, D.; Richardson, R.; Coy, R.; Schiller, U.D.; Chandrashekar, H.; Robertson, F.; Coveney, P.V. Validation of Patient-Specific Cerebral Blood Flow Simulation Using Transcranial Doppler Measurements. *Front. Physiol.* **2018**, *9*, 1–12. [[CrossRef](#)] [[PubMed](#)]
10. Westerhof, N.; Lankhaar, J.W.; Westerhof, B.E. The arterial windkessel. *Med. Biol. Eng. Comput.* **2009**, *47*, 131–141. [[CrossRef](#)]
11. Sagawa, K.R.; Lie, J. Schaefer, Translation of Otto Frank’s paper “Die Grundform des arteriellen Pulses” Zeitschrift fur Biologie 37: 483–526 (1899) [Translation of Otto Frank’s paper, The basic shape of the arterial pulse]. *J. Mol. Cell. Cardiol.* **1990**, *22*, 253–277. [[CrossRef](#)]
12. Mynard, J.P.; Davidson, M.R.; Penny, D.J.; Smolich, J.J. A simple, versatile valve model for use in lumped parameter and one-dimensional cardiovascular models. *Numer. Methods Biomed. Eng.* **2012**, *28*, 626–641. [[CrossRef](#)]
13. Walley, K.R. Left ventricular function: Time-varying elastance and left ventricular aortic coupling. *Crit. Care* **2016**, *20*, 626–641. [[CrossRef](#)]
14. Seemann, F.; Arvidsson, P.; Nordlund, D.; Kopic, S.; Carlsson, M.; Arheden, H.; Heiberg, E.; Noninvasive quantification of pressure-volume loops from brachial pressure and cardiovascular magnetic resonance. *Circ. Cardiovasc.* **2019**, *12*, e008493. [[CrossRef](#)] [[PubMed](#)]
15. Available online: <https://models.physiomeproject.org/welcome> (accessed on 1 May 2023).
16. Czechowicz, K.; Archer, G.; Franz, J.; Nowakowski, P.; Narracott, A.J.; Hose, D.R. *Modelling the Aortic and Mitral valve replacement using personalised 0D and 3D Computational Models of Left Heart Circulation*; To be submitted to Fluids; Multi-Disciplinary Publishing Institute: Basel, Switzerland, 2023.
17. Hann, C.E.; Chase, J.G.; Desai, T.; Froissart, C.; Revie, J.; Stevenson, D.; Lambermont, B.; Ghuyssen, A.; Kohl, P.; Shaw, G.M.; Unique parameter identification for cardiac diagnosis in critical care using minimal data sets. *Comput. Methods Programs Biomed.* **2010**, *29*, 75. [[CrossRef](#)]
18. Ramanathan, T.; Skinner, H. Coronary blood flow. *Contin. Educ. Anaesth. Crit. Care Pain* **2005**, *5*, 61–64. [[CrossRef](#)]
19. Wiggers, C. *Modern Aspects of the Circulation in Health and Disease*; Lea and Febiger: Philadelphia, PA, USA, 1923.
20. Monge Garcia, M.I.; and Santos, A. Understanding ventriculo-arterial coupling. *Ann. Transl. Med.* **2020**, *8*, 795–805. [[CrossRef](#)] [[PubMed](#)]
21. Stergiopoulos, N.; Westerhof, B.E.; Westerhof, N. Total arterial inertance as the fourth element of the windkessel model. *Am. J. Physiol.* **1999**, *276*, 81–88. [[CrossRef](#)] [[PubMed](#)]
22. Bastos, M.B.; Burkhoff, D.; Maly, J.; Daemen, J.; den Uijl, C.A.L.; Ameloot, K.; Lenzen, M.; Mahfoud, F.; Zijlstra, F.; Schreuder, J.J.; et al. Invasive left ventricle pressure-volume analysis: Overview and practical clinical implications. *Eur. Heart J.* **2020**, *21*, 1286–1297. [[CrossRef](#)]
23. Kunkel, P.; Mehrmann, V.L. *Differential-Algebraic Equations: Analysis and Numerical Solution*; European Mathematical Society: Zurich, Switzerland, 2006; ISBN 978-3-03719-017-3.
24. Jacobs, O.L.R. *Introduction to Control Theory*; Oxford University Press: Oxford, UK, 1984; ISBN 0-19-856148-2.
25. Murray, C.D.; The Physiological Principle of Minimum Work: I. The Vascular System and the Cost of Blood Volume. *Proc. Natl. Acad. Sci. USA* **1923**, *12*, 207–214. [[CrossRef](#)]
26. Huo, Y.; Kassab, G.S.; Intraspecific scaling laws of vascular trees. *J. R. Soc. Interface* **2012**, *9*, 190–200. [[CrossRef](#)]
27. Gosling, R.C.; Study, J.; Morris, P.D.; Fossan, F.E.; Hellevik, L.R.; Lawford, P.; Hose, D.R.; Gunn, J.P.; Effect of side branch flow upon physiological indices in coronary artery disease, *J. Biomech.* **2020**, *103*, 109698. [[CrossRef](#)]
28. Foerstermann, U.; Muenzel, T. Endothelial Nitric Oxide Synthase in Vascular Disease From Marvel to Menace. *Circulation* **2006**, *113*, 1708–1714. [[CrossRef](#)]
29. Linke, A.; Erbs, S.; Hambrecht, R. Effects of exercise training upon endothelial function in patients with cardiovascular disease. *Front Biosci.* **2008**, *13*, 424–432. [[CrossRef](#)]
30. Laufs, U.; Wassmann, S.; Czech, T.; Muenzel, T.; Eisenhauer, M.; Boehm, M.; Nickenig, G. Physical inactivity increases oxidative stress, endothelial dysfunction, and atherosclerosis, Arteriosclerosis. *Thromb. Vasc. Biol.* **2005**, *25*, 809–814. [[CrossRef](#)]
31. Sattelmair, J.; Pertman, J.; Ding, E.L.; Kohl, H.W.; Haskell, W.; and Lee, I.M.; Dose response between physical activity and risk of coronary heart disease: A meta-analysis. *Circulation* **2011**, *124*, 789–795. [[CrossRef](#)]
32. Hung, R.K.; Al-Mallah, M.H.; McEvoy, J.W.; Whelton, S.P.; Blumenthal, R.S.; Nasir, K.; Schairer, J.R.; Brawner, C.; Alam, M.; Keteyian, S.J.; et al. Prognostic value of exercise capacity in patients with coronary artery disease: The FIT (Henry Ford Exercise Testing) project. *Mayo Clin. Proc.* **2014**, *89*, 1644–1654. [[CrossRef](#)] [[PubMed](#)]
33. Hambrecht, R.; Walther, C.; Moebius-Winkler, S.; Gielen, S.; Linke, A.; Conradi, K.; Erbs, S.; Kluge, R.; Kendziorra, K.; Sabri, O.; et al. Percutaneous coronary angioplasty compared with exercise training in patients with stable coronary artery disease: A randomized trial. *Circulation* **2004**, *109*, 371–378. [[CrossRef](#)]

34. Shi, Y.; Korakianitis, T. Numerical simulation of cardiovascular dynamics with left heart failure and in-series pulsatile ventricular assist device. *Artif. Organs* **2006**, *30*, 929–948. [[CrossRef](#)]
35. Arts, T.; Bovendeerd, P.H.M.; Prinzen, F.W.; Reneman, Relation between left ventricular cavity pressure and volume and systolic fiber stress and strain in the wall. *Biophys. J.* **1991**, *59*, 93–102. [[CrossRef](#)]
36. Bovendeerd, P.H.; Borsje, P.; Arts, T.; van de Vosse, F.N. Dependence of intramyocardial pressure and coronary flow on ventricular loading and contractility, a model study. *Ann. Biomed. Eng.* **2006**, *34*, 133–1145. [[CrossRef](#)] [[PubMed](#)]
37. Li, R.; Henson, M.A.; Kurtz, M.J. Selection of model parameters for off-line parameter estimation. *IEEE Trans. Control. Syst. Technol.* **2004**, *12*, 402–412. [[CrossRef](#)]
38. Bjordalsbakke, N.I.; Sturdy, J.T.; Hose, D.R.; Hellevik, L.R. Parameter estimation for closed loop lumped parameter models in the systemic circulation using synthetic data. *Math. Biosci.* **2002**, *343*, 108731. [[CrossRef](#)] [[PubMed](#)]

Disclaimer/Publisher’s Note: The statements, opinions and data contained in all publications are solely those of the individual author(s) and contributor(s) and not of MDPI and/or the editor(s). MDPI and/or the editor(s) disclaim responsibility for any injury to people or property resulting from any ideas, methods, instructions or products referred to in the content.